Montanuniversität Leoben

Comparison of $Ti_{1-X}Al_XN$ coatings deposited by reactive magnetron sputtering from powder metallurgical targets and from mosaic targets

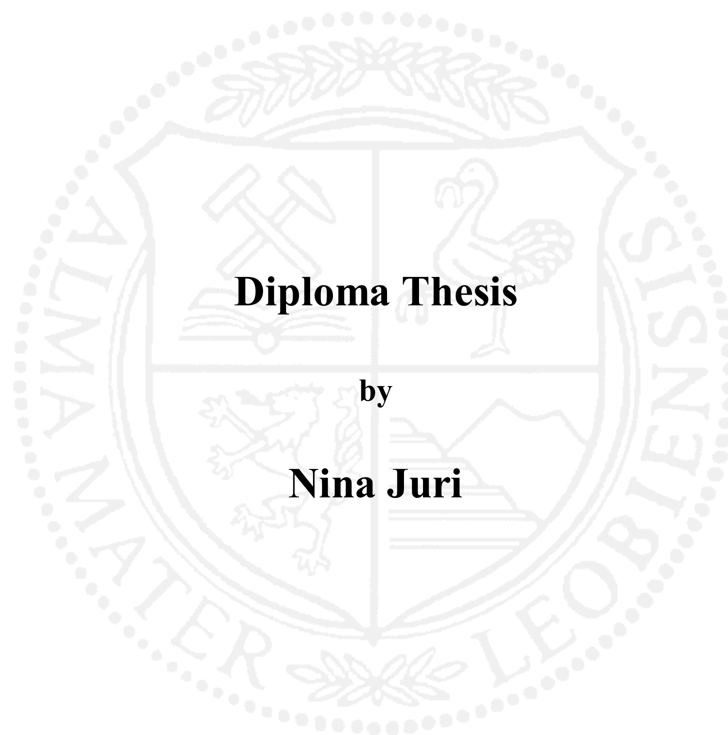

Diploma Thesis

by

Nina Juri

This work has been carried out within the Research Studio Austria Surface Engineering at the Department of Physical Metallurgy and Materials Testing, University Leoben, Austria.

Leoben, June 2010

Affidavit

I declare in lieu of oath, that I wrote this thesis and performed the associated research myself, using only literature cited in this volume.

Leoben, June 2010

Acknowledgments

I would like to thank o. Univ. Prof. DI Dr. Helmut Clemens, head of the Department of Physical Metallurgy and Materials Testing, for the possibility to compose this thesis at his department.

I am deeply grateful to a.o. Univ. Prof. DI Dr. Christian Mitterer, head of the Thin Film Group at the Department of Physical Metallurgy and Materials Testing, for his supervision and all the knowledge he was able to impart to me and especially for the confidence he places in me.

Furthermore, I am very grateful to my supervisor DI Thomas Weirather for his advice and his endless patience.

I would also like to express my gratitude to DI (FH) Conrad Polzer and Dr. Peter Polcik from PLANSEE Composite Materials, for providing the powder metallurgical targets for this work.

I also appreciate the great support through the team of the Thin Film Group. Thanks for your great support whenever needed and the pleasurable working atmosphere.

I am deeply indebted to my parents Dorothea and Rudolf for their valuable and enduring support.

Furthermore, I appreciate the real and loyal friendship with my brother Patrick. It is comforting and encouraging to know, that such an exceptional person stands at one's side.

I would also like to express my thankfulness to all those friends, who remain unnamed, but who have also made their contribution to my achievements.

Last but not least I would like to express my gratitude to Peter, my tower of strength. I wish to thank you for your great mental support, for the trust you place in me, for the countless encouragements you bestow upon me and especially for all the love you give to me.

Table of Contents

1 Introduction 1

2 Physical Vapor Deposition 3

2.1 Fundamentals of Physical Vapor Deposition 3

2.2 Sputtering 4

2.2.1 RF Sputtering 5

2.2.2 Bias Sputtering 6

2.2.3 Pulsed DC Sputtering 7

2.2.4 Magnetron Sputtering 7

2.2.5 Reactive Sputtering 9

3 Thin Film Growth 10

3.1 Nucleation and Growth 10

3.2 Structure Zone Models 11

4 Tribological Properties 15

4.1 Friction 15

4.2 Wear 17

5 TiAlN Coating Fundamentals 19

5.1 Crystal Structure 19

5.2 Mechanical Properties 22

5.3 Tribological Properties 23

6 Experimental Details 25

6.1 Targets 25

6.2 Substrates 25

6.3 Coating Deposition 26

6.4 Simulation of sputter process 27

6.5 Coating Characterization 28

6.5.1 Coating Thickness 28

6.5.2 Chemical Composition 29

6.5.3 Microstructure 29

6.5.4 Film Adhesion 31

6.5.5 Hardness and Young's Modulus 32

6.5.6 Coating Stress 33

6.5.7 Tribological Properties 34

7 Results and Discussion 35

7.1 Cathode Power and Nitrogen Partial Pressure Variation 35

7.2 Sputter Behavior 38

7.2.1 Coating Thickness and Deposition Rate 38

7.2.2 SRIM Simulation 41

7.3 Chemical Composition 43

7.4 Microstructure 44

7.4.1 Preferred Orientation 46

7.4.2 Domain size and Stress 47

7.5 Coating Adhesion 48

7.6 Residual Stress 49

7.7 Hardness and Young's Modulus 49

7.8 Tribological Properties 50

8 Summary and Conclusions 54

Bibliography 56

1 Introduction

High technology applications require special material properties which can not be satisfied by the bulk material solely. To achieve surface properties that differ from those of the bulk material, thin film technologies are used. The deposition of hard thin films on a substrate is, for example, a common technology to improve the performance of cutting tools but also of various dies and molds. One of the various methods for depositing a thin film on a substrate is physical vapor deposition (PVD) which is widely used to produce wear protective coatings [1].

To further increase the profitability, the industry demands a reduction of costs and consequently a reduction of machining time [2]. This affects on the one hand the cutting parameters, which need to be increased, and therefore also the development of hard coatings, which need to be improved to extend the lifetime of the tools. On the other hand, the coatings also need to be deposited efficiently. For that reason the deposition process has to be optimized, where the required targets play a decisive role.

There are various kinds of targets for sputter processes applied in industry, which can be synthesized by different processing techniques. For the present work, powder metallurgically produced targets were compared with mosaic targets. The powder metallurgical targets were titanium aluminum targets consisting of separated titanium and aluminum phases, where titanium grains are embedded in an Al matrix. The mosaic targets are cast and made of pure titanium with drilled holes which are filled with aluminum inserts. In either case the total thickness is 10 mm, but in case of the powder metallurgical targets the usable sputter area is 10 mm thick, while in case of the mosaic targets the compound is just 6 mm thick and fixed on a 4 mm thick copper back plate. Therefore, the erosion track of the powder metallurgical targets can be deeper and consequently the target lifetime is longer. To elucidate if there are further advantages of the powder metallurgical targets in comparison to the mosaic targets, coatings are deposited on high speed steel substrates and subsequently characterized.

However, with the utilized industrial-size sputter device up to date only mosaic targets have been used. Thus, first of all, the deposition process has to be optimized for the powder metallurgical targets. For that reason, variations of the target sputter power and the nitrogen partial pressure have to be done. For the deposition of the coating with the mosaic targets, a well established standard process is available.

The implemented sputter process for the powder metallurgical targets is compared within this thesis to the commercially applied mosaic target process by taking into account the sputtering yields of Ti and Al and the respective deposition rates. A higher deposition rate reduces the

process time needed to obtain the desired film thickness. Thus it is preferable with respect to the efficiency of the coating process.

As coating properties are strongly influenced by the deposition parameters, the obtained coatings are compared to each other with respect to their thickness, structure, preferred orientation, domain size, film adhesion, hardness, Young's modulus, residual stresses and tribological properties.

2 Physical Vapor Deposition

2.1 Fundamentals of Physical Vapor Deposition

Hard coatings provided by physical vapor deposition (PVD) on cemented carbide or high speed steel (HSS) substrates are well established in wear protection [1]. PVD comprises different deposition techniques which are all based on the same three main steps:

1. Formation of vapor
2. Transportation of the vapor from source to substrate
3. Condensation, nucleation and growth of the film on the substrate

Due to the different physical methods of transferring the material which should be deposited to vapor a classification of PVD processes can be done (fig. 2.1):

- Evaporation (thermal, e.g. electron beam, laser beam, arc discharge)
- Sputtering (bombardment of the solid deposition material with positive gas ions)
- Ion Plating (combination of evaporation and sputtering, ion bombardment of the substrate to improve the properties of the film)

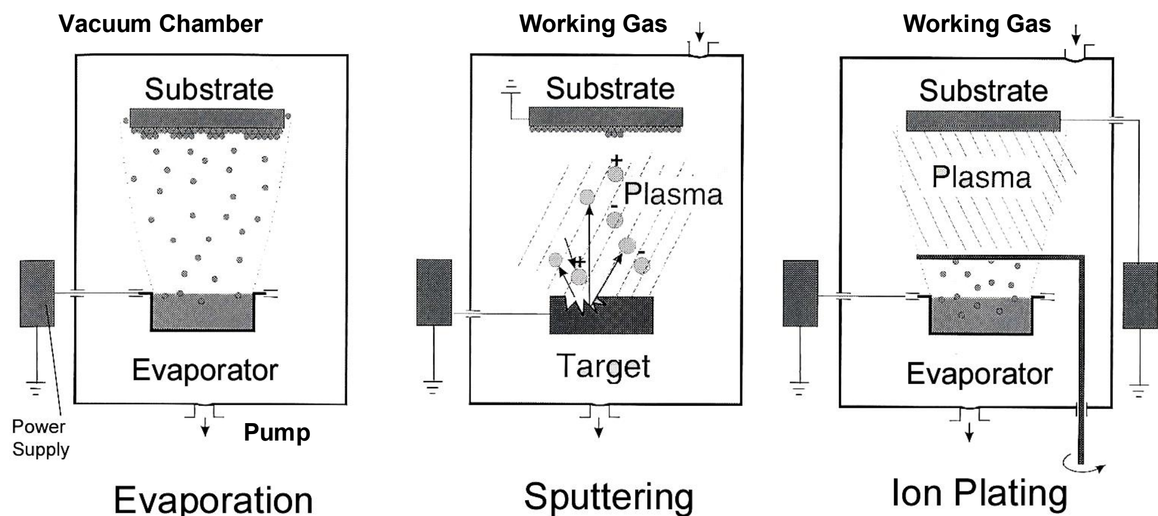

Fig. 2.1: Schematic description of the three basic PVD processes [3].

The outstanding qualities of these processes are the versatility of both potential substrate and potential film materials. It is possible to deposit nearly every kind of inorganic materials (e.g. metals, alloys, compounds), as well as several organic materials [4]. All three PVD processes offer the alternative of reactive deposition; i.e., that a reactive gas is injected into the vacuum chamber which forms a chemical compound with the evaporated or sputtered material [5],

resulting in a wide range of possible compositions of the film. Another benefit is the high process flexibility which can affect the microstructure significantly. Besides, PVD-coatings exhibit an excellent bonding to the substrate and can be deposited at very low process temperatures [4]. The thickness of the film can vary from several Ångstrom to a few millimeters at sputtering rates in the range of Ångstrom up to 75 µm per minute [4].

The films deposited and analyzed for this diploma thesis were produced by sputter deposition. Thus, the following discussion is focused on this method.

2.2 Sputtering

In sputter deposition processes the solid deposition material, called *target*, is transferred to the vapor state by bombarding its surface with energetic ions (e.g. Ar^+). This procedure is based on energy and momentum transfer from the impinging ions to the surface atoms of the target. There are several possibilities of interaction, for example direct ejection of surface atoms or the possibility of a sequence of collisions between ions and atoms or atoms among each other (fig. 2.2). If the energy of the scattered atoms of the collision sequence is higher than the surface binding energy, surface atoms can be ejected. The ejected particles are mainly neutrals. The number of target atoms ejected per incident ion is termed sputtering yield [4, 6].

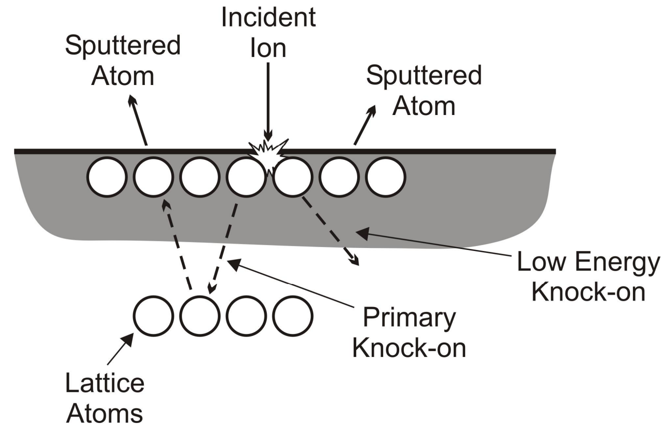

Fig. 2.2: Schematic of the basic momentum transfer processes during sputtering [4].

In fig. 2.3 the setup of a DC sputtering system is shown. As indicated, the target and the substrate are positioned in a high or ultrahigh vacuum chamber. To provide the ion bombardment, inert gas is induced to the vacuum chamber until pressures of about 0.1 to 1 Pa are achieved. Then a *glow discharge* is ignited by applying a voltage of 0.5 to 5 kV between the target, which acts as the cathode, and the substrate holder, which acts as the anode. In this way ionization of the working gas is achieved in the surrounding of the target. This ionized working gas is called *plasma* [4].

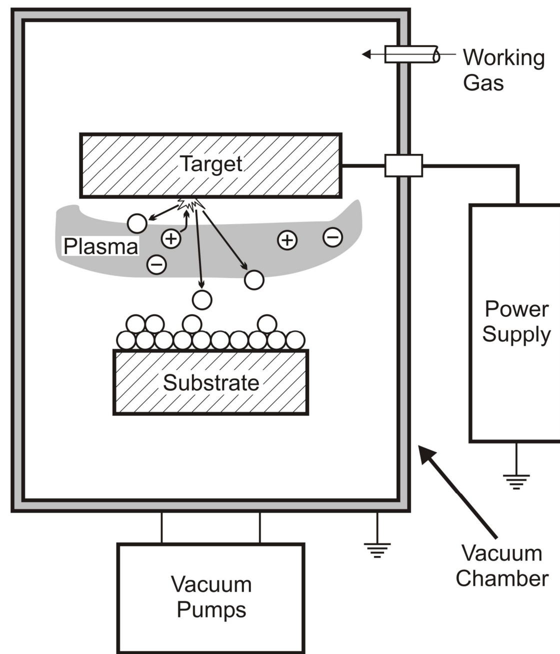

Fig. 2.3: Schematic of the sputter deposition process [4].

A major attribute of sputtering versus e.g. arc evaporation is that the evaporation in case of sputtering is achieved by momentum transfer and not thermally, so almost every material can be sputtered. By applying a DC voltage only metals can be sputtered, whereas with an RF (radio frequency) voltage non-conducting as well as conducting or semiconducting materials can be sputtered [5]. Another method of sputtering less conductive materials is pulsed DC sputtering.

2.2.1 RF Sputtering

In order to have the possibility to deposit also insulating materials, RF sputtering was developed. There, an RF field is required which can be produced in two possible ways. One is to use an inductor. The other, and more common, possibility is to assemble two cathodes in the recipient and apply a radio frequency voltage. In this case one of the cathodes is coupled with a capacitor. This method is based on the fact, that any surface that is capacitively coupled to the plasma is charged negatively relative to the plasma. As a result of their higher mobility, more electrons reach the electrode at the positive half-wave, than ions at the negative half-wave. Thus, the electrode is negatively charged compared to the plasma. This is also called self-biasing. If the radio frequency is sufficiently high, the ions cannot follow the temporal variations of the voltage. In this way the target is continuously bombarded by ions, while only during the short time when the target is positively compared to the plasma a lot of electrons flow as a displacement current. Due to this displacement current also insulators and semiconductors can be sputtered.

RF-sputtering is widely used for producing multilayer coatings in semiconductor technology. In this case there are two to four RF-targets assembled in the vacuum chamber [5, 7].

2.2.2 Bias Sputtering

In standard sputter deposition processes the substrate table is grounded. In case of bias sputtering, a negative DC voltage (fig. 2.4a) of about 50 to 100 V is applied to the substrate table, such that the substrate is on negative potential compared to the plasma. Thereby, the growing film is constantly bombarded with ions from the sputter gas and impurities are removed. The impinging ions could, to a certain extent, be integrated into the film, which can be a disadvantage. However, due to these impinging ions local heating of the substrate, called atomic scale heating, is caused [5]. This local heating affects the mobility of the condensed particles positively and thus enhanced film properties can be achieved [5, 6, 7, 8].

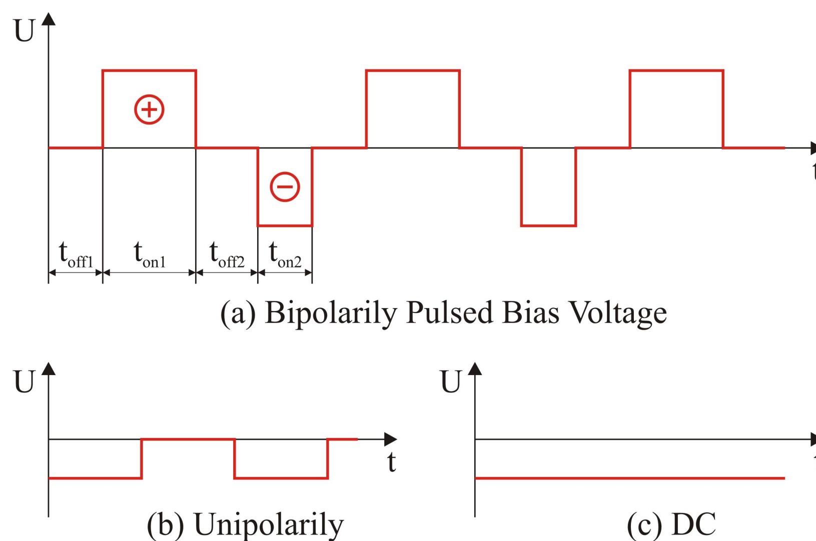

Fig. 2.4: Voltage/time diagram of (a) a bipolarily pulsed bias voltage, (b) a unipolarily pulsed bias voltage and (c) a negative DC voltage [10].

A further improvement of the sputter deposition process is the so called pulsed bias sputtering. There a pulse modulator is used, which biases the substrates using short-duration, repetitive (100 Hz to kHz range) voltage pulses. The ratio between the time the bias is on to the total time of a pulse cycle is called duty cycle. Charged particles are accelerated to the substrate only during the time the bias is on. According to figure 2.4 a distinction has to be made between unipolarily and bipolarily pulsed bias voltage. In the case of unipolarily pulsed negative bias voltage, the modulator biases the part to a high, negative potential (typically in the range of 20 – 250 V). Thus it is possible to reduce the average substrate temperature due to the reduction of the total ion-bombardment time [9]. By applying a bipolarily pulsed bias voltage the substrate is alternately biased to a high positive and to a high negative potential. By the time the substrate is on negative potential, the growing film is again bombarded with

positive ions. On the other hand, while it is on positive potential, the film is bombarded with electrons. This electron treatment does not influence the overall substrate temperature. The advantage of using a pulsed bias source is that it is possible to deposit with higher bias voltages, at lower temperature and to achieve dense films with beneficial properties such as e.g. microstructure, film uniformity, adhesion and internal stress [9, 10, 11, 12].

2.2.3 Pulsed DC Sputtering

Pulsed DC sputtering is a further method for depositing insulating materials. Virtually it is a combination between DC sputtering and RF sputtering. Pulsed DC sputtering is based on the addition of a reverse voltage pulse to the normal DC waveform. As with RF sputtering, the frequency has to be high enough so that the ions cannot follow the temporal variations of the voltage. Pulse frequency and duty cycle can be varied to optimize the process. In the case of pulsed DC sputtering, the cathodes are run with a pulsed DC power supply. The typical frequency range is 10 kHz – 350 kHz. Similar to pulsed bias sputtering a distinction has to be made between bipolarily and unipolarily pulsed DC voltages (fig. 2.4) [13, 14].

2.2.4 Magnetron Sputtering

During magnetron sputtering a magnetic field **B** is applied in the area between the target and the substrate. Employing this field the electrons are trapped adjacent to the target. In this way the ionization rate in this area can be increased, which consequently leads to increased sputtering rates and finally results in increased film growth rates.

The magnetic field **B** is produced by permanent magnets which are located behind the targets, in a so-called magnetron. This field **B** superimposes the electric field **E** of the glow discharge. As a consequence of the so called **ExB** drift, the charged particles are forced to follow a closed-loop helical path along the magnetic field lines. Due to their higher mass, the ions are hardly influenced by the magnetic field and follow a more distant path. Thus, only the electrons are confined near the target, forming a circular current, also called race track. Together with the electrons of the plasma secondary electrons, generated by ions impinging on the target, are concentrated near the target. Due to the high electron concentration, more sputter gas atoms are ionized. In consequence of the high ionization rate, the sputter erosion of the target takes place mainly within the area of the race track [6, 15].

It can be distinguished between balanced and unbalanced magnetrons (fig. 2.5). The assemblies differ in the course of the magnetic field lines between the outer and the inner magnets. In a balanced magnetron (fig. 2.5a) all magnetic field lines loop above the target. An unbalanced magnetron (fig. 2.5b) is an assembly where the outer or inner magnet is stronger than

the other one so that not all magnetic field lines loop between them. As a result there are magnetic field lines which reach the substrate. Thus, the ionization rate in the area near the substrate increases and the growing film is bombarded by low-energy ions and electrons. The mobility of the condensed particles on the substrate increases, resulting in improved film properties [6, 8].

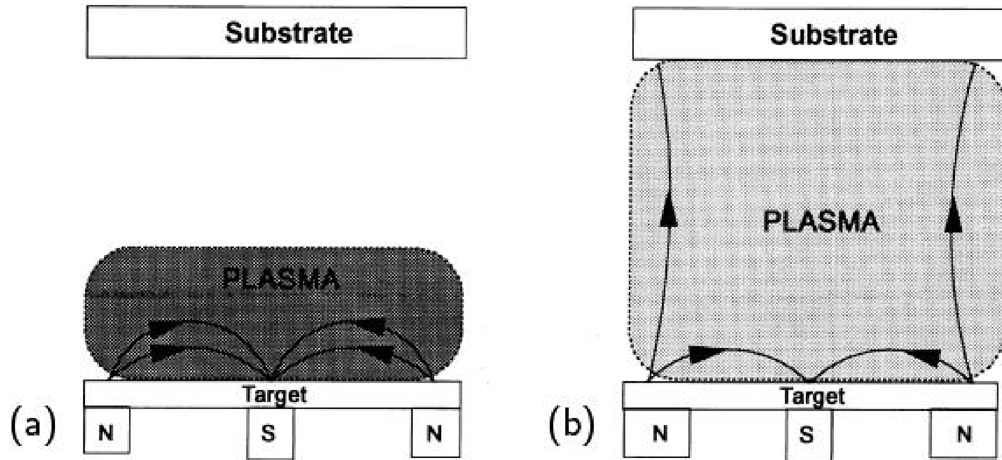

Fig. 2.5: Schematic of (a) a balanced and (b) an unbalanced magnetron [16].

In fig. 2.6 a balanced magnetron in circular planar configuration is shown. The closed loop magnetic field lines, the area of erosion and the helical motion of the electrons as described above are indicated.

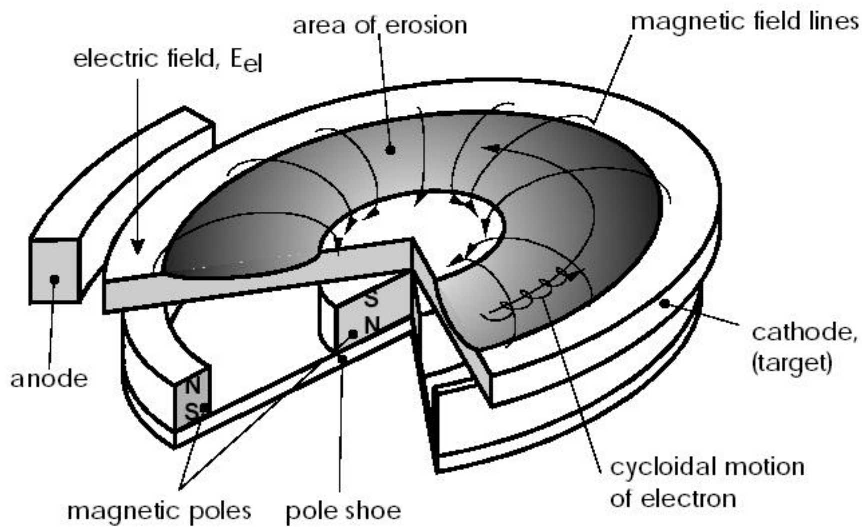

Fig. 2.6: Schematic of a planar magnetron in circular configuration [17].

2.2.5 Reactive Sputtering

Among several other possibilities, such as multicomponent targets and different single element targets, reactive sputtering is used to deposit alloys.

There, not all atoms of the film originate from the target, but at least one component of the film originates from the gas phase. A particular fraction of reactive gas, for example nitrogen N_2, is induced into the vacuum chamber additionally to the inert working gas. Three different reactions are possible to form the compound [6, 7, 15, 18]:

1. Formation of the compound at the surface of the target and sputtering of this molecules
2. Formation of a compound in the gas phase
3. Adsorption of the reactive gas on the substrate and subsequent reaction with impinging atoms of the target

Since compounds formed on the target surface are assumed to be sputtered as single atoms and because of the low probability of collisions between sputtered atoms, reactive gas molecules and ions/electrons (needed to provide the energy for compound formation) in the gas phase, reaction 3 is the most important one for compound film formation.

A benefit of reactive sputtering is that the stoichiometry of the deposited film can be modified by adjusting the partial pressure of the reactive gas. With reactive sputtering it is possible to fabricate various, even very complicated, compounds by employing simple metallic targets and providing the other components in the gas phase [5, 7].

A disadvantage of reactive sputtering is the formation of compound films on the target surface, often resulting in lower sputtering rates (i.e., the so-called target poisoning) [19].

3 Thin Film Growth

3.1 Nucleation and Growth

After evaporation and transportation of the vapor from the target to the substrate, the sputtered atoms collide with the solid surface of the substrate. There they are either reflected or, if they transfer enough energy to the substrate lattice, they become loosely bonded (fig. 3.1). These loosely bonded atoms are called *adatoms*. The adatoms diffuse over the surface until they are either desorbed, by re-evaporation or back-sputtering, or they reach other adatoms. In the second case the adatoms build stable nuclei or condense at already existing nuclei. The first process is termed nucleation. The nuclei are preferably formed at low energy sites, like for example at steps, scratches or lattice defects in the surface. The mobility of the adatoms on the substrate surface depends on their kinetic energy, the substrate temperature and on the intensity of interactions between adatoms and substrate. If these interactions are strong, the nucleation density is high and likewise, if the interactions are weak, the nucleation density is low. Higher nucleation density causes a bigger contact area between coating and substrate and simultaneously lesser cavities in the interface and thus better adhesion is achieved [4, 5].

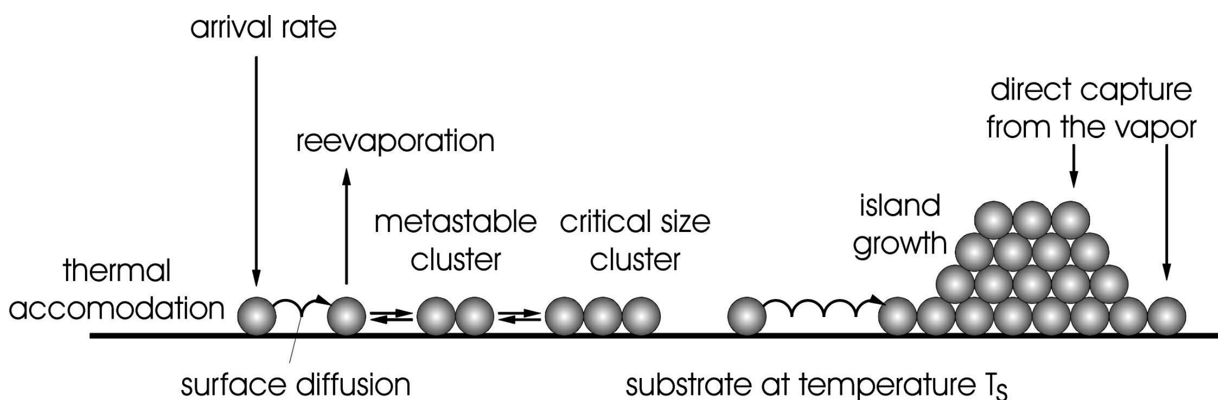

Fig. 3.1: Schematic of nucleation and growth processes on a solid surface [17].

Further enlargement of the nuclei proceeds similarly to the nucleation process, by adatoms impinging directly on the nuclei or diffusion of adatoms over the surface to the nuclei. This enlargement of nuclei is termed growth [4]. There are three basic growth modes observed: Island growth (or Volmer-Weber mode), layer-by-layer growth (or Frank-van der Merwe mode), and mixed layer-island growth (Stranski-Krastanov mode). In fig. 3.2 these growth modes are depicted schematically [15].

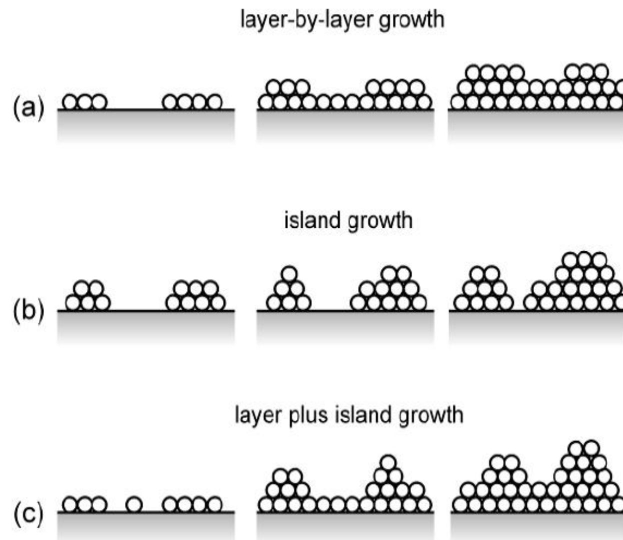

Fig. 3.2: Schematic of thin film growth modes: (a) layer-by-layer growth, (b) island growth and (c) mixed layer-island growth [15, 20].

Island growth occurs when the binding energy between the adatoms is stronger than between the adatoms and the substrate. In layer growth the opposite happens. Here the adatoms are more strongly bound to the substrate than to each other. If one monolayer is completed it is covered with a second layer and so on. The mixed layer-island growth is a combination of the other two modes. There, one or more monolayers are formed, but then further layer growth becomes unfavorable and islands are formed [15].

3.2 Structure Zone Models

The properties of thin films provided by PVD processes are determined by their microstructure, where the microstructure is highly dependent on the preparation parameters. Thus, it is essential to know about the relations between the microstructure and the deposition parameters [21].

Movchan and Demchishin were the first to propose a *structure zone model* (SZM), which relates these dependencies. They investigated very thick (up to 2 mm) vapor deposited coatings of different materials and related their morphological structure to the homologous temperature (T_s/T_m), where T_s is the substrate temperature and T_m is the melting temperature. They found three characteristic structure zones [5, 22].

Thornton adapted this structure zone model for sputter deposited metal coatings by introducing a second variable additional to the homologous temperature, the inert sputtering gas pressure. In Thornton's model (fig. 3.3a) a fourth zone, the so called Transition Zone (Zone T) is considered to be between Zone 1 and Zone 2 [23].

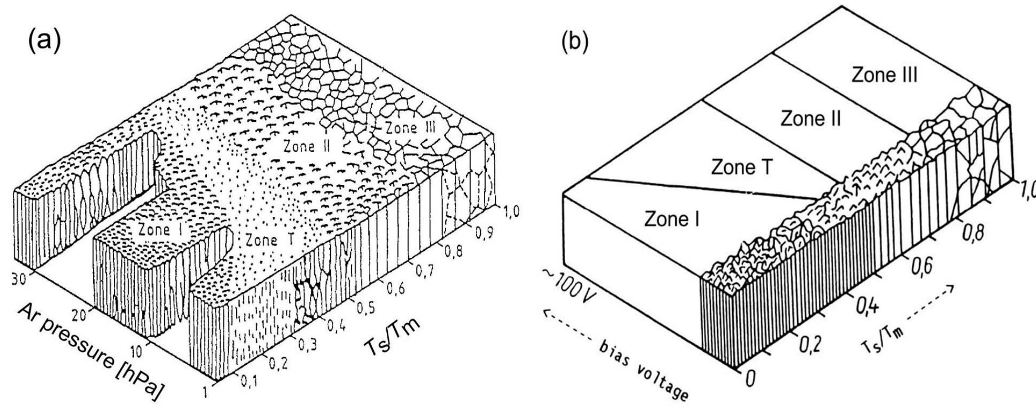

Fig. 3.3: Structure zone models proposed by (a) Thornton [23] and (b) Messier *et al.* [21].

Messier *et al.* proposed a further model (fig. 3.3b) adapted for thin films, in which the bias potential is considered as well [21].

In **Zone 1** the homologous temperature T_s/T_m is very low (< 0.2). There is little adatom surface mobility and therefore the growth is affected significantly by shadowing effects. The microstructure is characterized by tapered crystallites and voids between them. **Zone T**, which is considered to be a transition zone between Zone 1 and Zone 2, belongs to the temperature interval $0.2 < T_s/T_m < 0.4$ and develops by competitive growth of differently oriented neighboring crystals. In this range there is distinct adatom surface diffusion and the shadowing effects are partially compensated. The structure is fibrous and denser than in Zone 1. In the temperature interval $0.3 < T_s/T_m < 0.5$ the effect of grain boundary migration becomes relevant. This marks the beginning of **Zone 2**. The surface mobility in this zone is even higher. The film is composed of columnar crystals expanding from the bottom to the top of the film and grain boundaries which are perpendicular to the substrate surface. The structure is homogeneous along the film thickness and the lateral size of the grains increases with increasing temperature. In **Zone 3**, which is marked by homologous temperatures higher than 0.5, the structure is characterized by equiaxed three dimensional grains. In this zone additional to the surface mobility, bulk diffusion becomes decisive. This results in recrystallization and further densification of the growing film [5, 23, 24].

It was observed by Thornton, that Zone T emerges when the sputtering gas pressure is decreased. Decreasing sputtering gas pressure causes increasing mean free paths of the particles, which consequently leads to an increased energy of the sputtered species as they arrive at the film surface and, therefore, to increased adatom mobility [21, 23].

Furthermore, according to Messier *et al.*, Zone T expands with increasing energy of the substrate bombarding ions. The increase of Zone T occurs mainly at the cost of Zone 1 while the Zone 2 boundary and its width remain nearly constant. Thus, densely packed fibrous grains can be observed already at lower temperatures. Apart from that fact the formation mechanism

of the film is very similar in Zone 1 and Zone T. For that reason Messier *et al.* considered Zone T to be an internal structure of Zone 1 [21].

The influence of the ion bombardment on the film structure can be explained by considering that the bombardment causes point defects on the substrate surface which lead to an increased nucleation density. On the other hand the impinging ions transfer energy to the adatoms which in turn leads to increased adatom mobility. Thus, at a given homologous temperature the crystal structure is denser if ion bombardment is applied, compared to the case without ion bombardment [5].

Barna *et al.* investigated the influence of impurity atoms on the structure zones. The co-deposition of active impurity species is hardly avoidable. But on the other hand, these so called impurities can also be alloying elements, and in this case they are intentionally introduced. However, these impurities play a major role in the structure formation of polycrystalline films. For that reason Barna *et al.* developed a so called real structure zone model (fig. 3.4) considering not only the substrate temperature but also the effect of impurities [24, 25, 26].

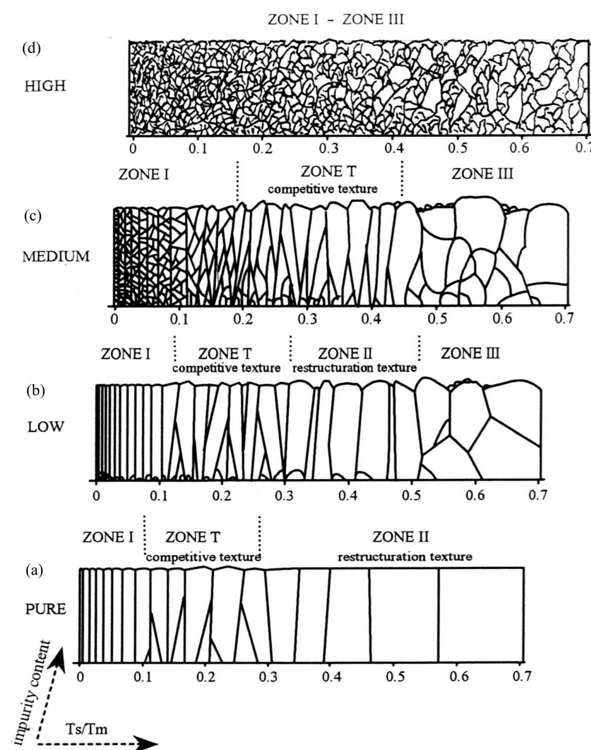

Fig. 3.4: Structure zone models modified with varying content of impurities. (a) ideal SZM, (b) real SZM of low, (c) medium and (d) high impurity concentration [26].

As indicated in fig. 3.4, the Zone 1 / Zone T boundary is shifted to higher temperatures with higher contamination content. Due to the low surface mobility of the impinging atoms no coalescence or grain boundary migration is possible in Zone 1 and thus, growth of large grains is

inhibited. In contaminated films, the Zone T / Zone 2 boundary is also shifted to higher temperatures because of limited grain boundary mobility. Nevertheless, in highly contaminated films (fig. 3.4d) the impurity phase can block the growth completely, consequently no competitive growth takes place and Zone T disappears. In pure films (fig. 3.4a) Zone 3 does not exist, while in contaminated films at high temperatures Zone 3 appears and represents thereby the upper boundary of Zone 2. However, if the contamination content is further increased the grain boundaries become immobile and Zone 2 does not appear (fig. 3.4c). The lower boundary of Zone 3 is shifted to lower temperatures with increasing contamination content. This initially leads to the disappearance of Zone 2 (fig 3.4c), later Zone T vanishes too (fig. 3.4d) and the lower boundary of Zone 3 reaches the upper boundary of Zone 1. The appearance of Zone 3 can be explained by process induced segregation of impurities. The impurity species are segregated on the growing surface of the crystal, resulting in a covering layer of impurities. Hence, the growth of individual crystallites is interrupted periodically and continues again by repeated nucleation [25, 26]. This process is used advantageously to deposit multi-component and multiphase films by using targets of different materials. According to the assembly of the targets it is possible to deposit multilayer films [5, 25].

4 Tribological Properties

The term tribology (greek τριβοσ: rubbing, sliding) was introduced to describe phenomena associated with interacting surfaces in relative motion. It comprises the topics of friction, wear and lubrication [27]. Tribological properties, such as e.g. the friction coefficient, are related to a system of materials, lubricants and other influence parameters as shown in fig. 4.1. This system is also referred to as tribosystem [28].

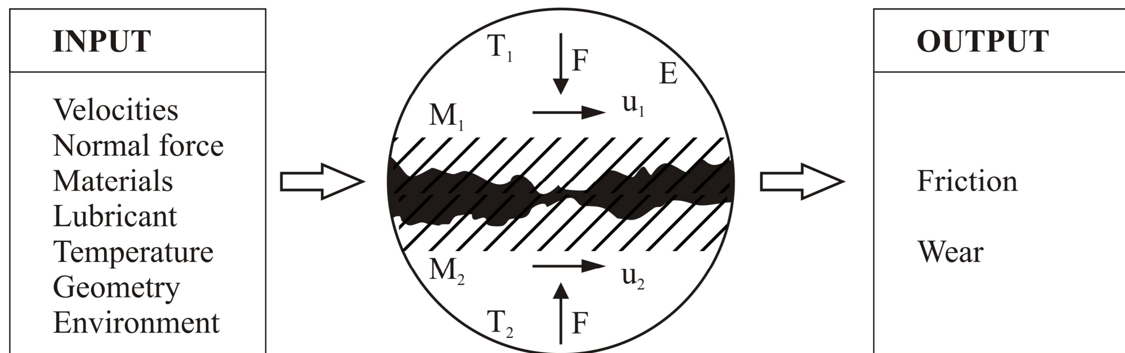

Fig. 4.1: Input and output parameters of a tribosystem [28].

4.1 Friction

According to ASTM, friction and friction force are defined as *resisting force tangential to the interface between two bodies when, under the action of an external force, one body moves or tends to move relative to the other* [29]. The friction coefficient μ is determined as the ratio between the frictional force F_R and the normal load F_N.

$$\mu = \frac{F_R}{F_N} [-] \tag{4.1}$$

The value of the friction coefficient describes the magnitude of the frictional force [30].

Two classes of relative motion, namely sliding and rolling have to be distinguished [30]. As rolling friction is not relevant for the present work, only sliding friction is discussed in more detail.

Bowden and Tabor (1950) explained the mechanism of sliding friction by the adhesional effect between surface asperities and also included the plowing effect in their concept. 1981 Suh and Sin [31] presented a new concept of friction, wherein three basic mechanisms are distinguished (fig. 4.2):

- Adhesion

- Plowing
- Asperity deformation

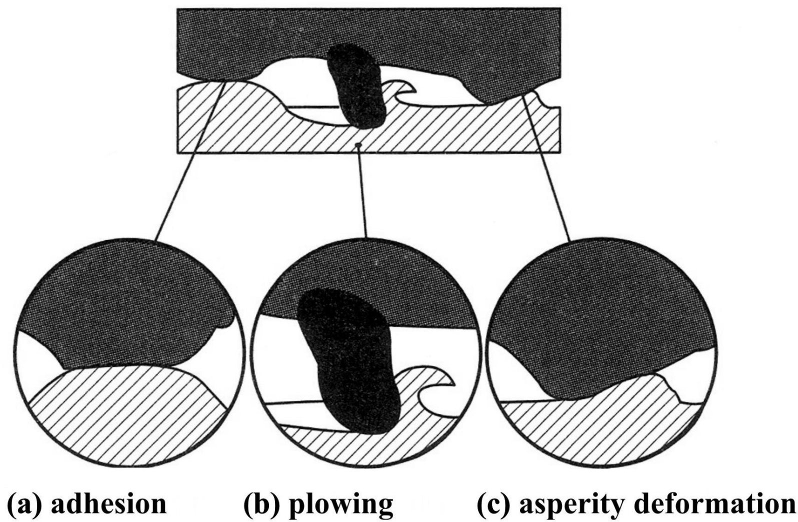

Fig. 4.2: The three basic mechanisms of sliding friction (a) adhesion, (b) plowing, (c) asperity deformation [28].

Adhesion

If two smooth, clean and oxide-free surfaces are in contact, there are areas of real contact, so called asperity junctions. The asperities are forced into contact and weld together (see fig. 4.2a). When two bodies in relative motion are slid over each other these junctions break. This recurring process causes a resistance to the motion [28, 30].

Plowing

When there are hard asperities or particles between the two surfaces in relative motion they can penetrate into the softer material. By moving one body relative to the other, a furrow is built by plastic flow (fig. 4.2b). This mechanism is called plowing and causes also a resistance to the motion [28].

Asperity Deformation

As depicted in fig. 4.2c, the surface asperities of two bodies in relative motion are elastically and plastically deformed as they slide over each other. The physical work performed hereby likewise contributes to the resistance to relative motion [28].

4.2 Wear

According to ASTM, wear is defined as the *damage to a solid surface, generally involving progressive loss of material, due to relative motion between that surface and a contacting substance or substances* [29].

There are various mechanisms which describe the possible ways of the loss of material on the surface of bodies in relative motion. In real contact more than one wear mechanism arises simultaneously. The four basic wear mechanisms are (fig. 4.3) [28, 32]:

- Adhesive wear
- Abrasive wear
- Fatigue wear
- Chemical wear

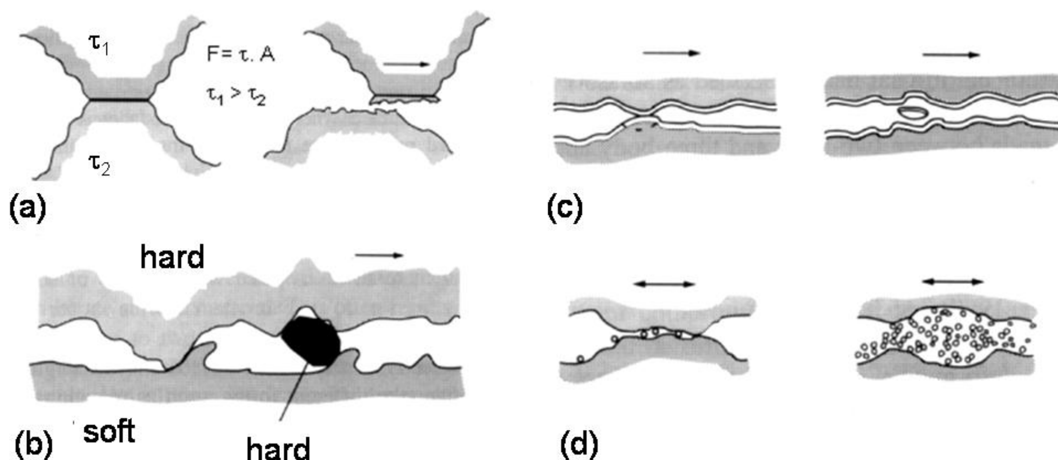

Fig. 4.3: Depiction of the different wear mechanisms: (a) adhesive, (b) abrasive, (c) fatigue and (d) chemical wear [28].

Adhesive Wear

When two smooth bodies are in contact, the asperities of one surface come into contact with asperities of the other surface (fig. 4.3a). These asperities in contact can adhere strongly to each other (compare the frictional adhesion mechanism in section 4.1). Through relative motion the majority of the softer asperities are separated and material is transferred to the counterpart (fig. 4.3a) [28, 32].

Abrasive Wear

When a rough hard surface or a surface containing hard particles is in contact with a softer surface, the harder surface asperities or particles are pressed into the softer surface (fig. 4.3b). By sliding of the bodies relative to each other, grooves and scratches are plowed in the softer material. Wear particles arise out of the displaced material from the grooves and scratches. Abrasive wear caused by hard surface asperities is also called two-body abrasive wear, while wear caused by hard particles in the tribological contact is called three-body abrasive wear. [28, 32].

Fatigue Wear

Fatigue wear results from repeated loading and unloading cycles of the surface at stress levels the material can sustain once but not if repeated several times. As a consequence of this loading and unloading cycles, surface or subsurface cracks can occur. As indicated in fig. 4.3c, these cracks will eventually result in the breakup of the surface with liberation of surface material acting as so called wear debris [28, 32].

Chemical Wear

Chemical wear is dominated by chemical reactions in the tribological contact in combination with mechanical contact mechanisms. Decisive for the chemical reactions are environmental influences. Most common in this field is oxidational wear. There, a thin layer of oxides is formed on the surface. This oxide film can act as a protecting layer against friction and wear of metals. When the two bodies in contact are moved relative to each other this protecting oxide layer can be continuously removed by the rubbing action. The surface is no longer protected and hence can be subject to increased wear. Additionally the removed material forms wear debris [28].

5 TiAlN Coating Fundamentals

Titanium nitride (TiN) coatings are widely used in various fields of application as for instance as diffusion barriers in microelectronics, as reflecting materials in the automobile and glass industry or as golden surface embellishing coatings in jewelry. However, their main field of application is their usage as hard and wear resistant coatings in the machining tool industry [33]. TiN films exhibit high hardness, relatively low friction, good corrosion resistance, good thermal conductivity and reasonable coating adhesion [34]. On the other hand they also show some drawbacks, e.g. their limited oxidation resistance. TiN films start to oxidize already at temperatures of about 550 °C forming rutile (TiO_2) [35].

Industrial demands for reduced machining time and consequently machining costs require increased cutting parameters. To fulfill these growing demands, TiN is more and more replaced by ternary compounds (e.g. TiAlN) for many applications [2].

By alloying aluminum to the TiN system, the mechanical properties such as hardness, coating adhesion and wear resistance can be enhanced further. Similar to the mechanical properties, the oxidation resistance remarkably increases with increasing Al content. In fact the start temperature for oxidation of $Ti_{1-X}Al_XN$ films can be increased significantly up to 950 °C for films containing 60 to 70 % Al. This outstanding oxidation resistance is caused by the formation of a stable oxidation barrier of Al_2O_3 at the surface. However, at temperatures above 950 °C a brittle underlayer of rutile is built, which may affect the performance of the protecting oxide layer [36, 37, 38].

5.1 Crystal Structure

In fig. 5.1 an isothermal cut through the ternary phase diagram Ti-Al-N at 1000 °C is shown. This diagram reveals that in thermodynamic equilibrium Ti, Al and N have virtually no or very low solubility in AlN, TiN and TiAl, respectively. However, two ternary phases exist, namely the cubic Ti_3AlN (perovskite structure) and the hexagonal Ti_2AlN phase, which is also called H phase [36, 39].

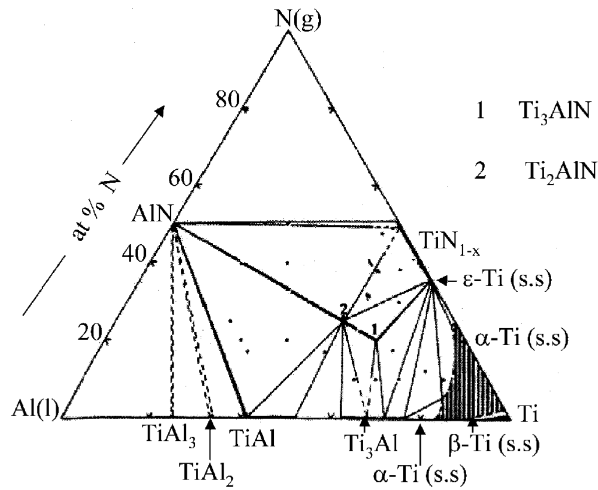

Fig. 5.1: Isothermal cut of the ternary phase diagram Ti-Al-N at 1000 °C [36].

Since the film growth of PVD coatings is based on free atoms and particles with simultaneous energy and momentum transfer, PVD thermodynamically is a non-equilibrium process. Therefore, the composition range of ternary films prepared by PVD is basically not limited by thermodynamics and it is possible to deposit metastable solid solutions [40, 41].

In fig. 5.2 the quasibinary phase diagram of TiN-AlN for thermal equilibrium as well as the PVD phase diagram for non-equilibrium processes is depicted. Again the low solubility of AlN in TiN in thermal equilibrium can be seen (fig. 5.2a). Besides, the maximum solubility (~ 5 %) is reached at very high temperatures and decreases with decreasing temperature. At room temperature a dual phase field of TiN and AlN is existing. TiN crystallizes in the face centered cubic (fcc) rock salt (NaCl) structure, while AlN crystallizes in the hexagonal close packed (hcp) wurtzite structure [36, 40, 42].

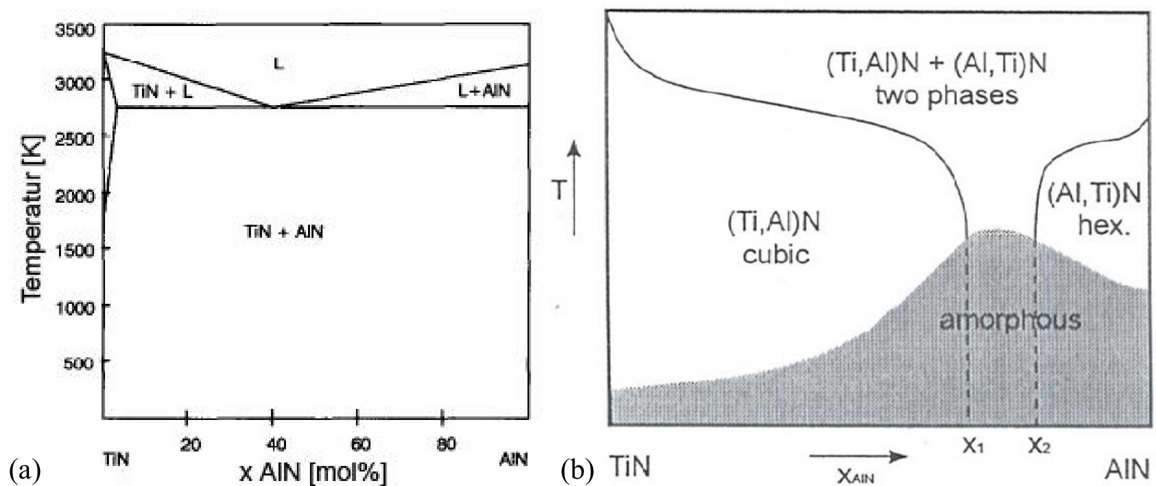

Fig. 5.2: (a) Quasibinary phase diagram of TiN-AlN [40], (b) phase diagram of TiN-AlN for non-equilibrium processes [43].

In contrast, fig 5.2b shows the $Ti_{1-X}Al_XN$ phase diagram for non-equilibrium processes. Via PVD it is possible to prepare supersaturated metastable solutions. Thus, cubic as well as hexagonal solid solutions can be built. According to fig. 5.2b, the two single-phase regions for fcc and hcp $Ti_{1-X}Al_XN$ are separated by a two-phase region, which expands with increasing substrate temperature [41, 43, 44].

As indicated in fig. 5.3, the formation of fcc $Ti_{1-X}Al_XN$ is based on the substitution of Ti atoms by Al atoms. Single-phase fcc $Ti_{1-X}Al_XN$ is formed up to Al contents x of approximately 0.6 to 0.67. Further increasing of the AlN mole fraction yields a dual-phase (fcc and hcp) structure followed by single-phase wurtzite $Ti_{1-X}Al_XN$, where the Ti atoms substitute the Al atoms in the hexagonal AlN lattice [36].

According to Vegard's law, the incorporation of Al in the fcc TiN lattice causes a reduction of the lattice parameter from 4.23 Å for pure TiN to 4.17 Å for an Al content of x=0.6 [45].

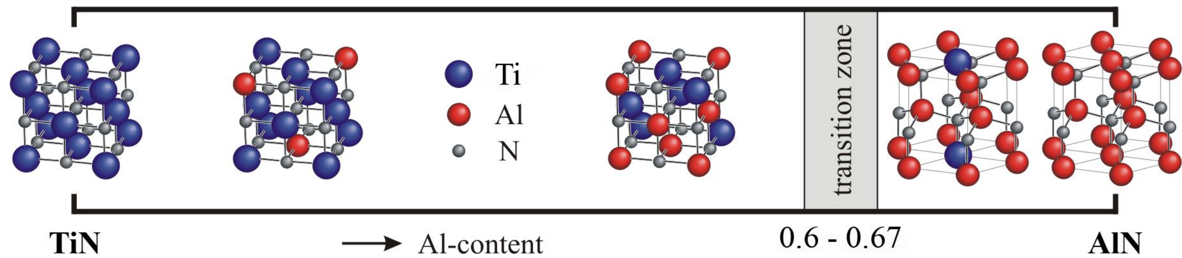

Fig. 5.3: Structural development of $Ti_{1-X}Al_XN$ with increasing Al-content [20, 39, 46].

Since $Ti_{1-X}Al_XN$ is a metastable solid solution, decomposition occurs at elevated temperatures by a spinodal process. Spinodal decomposition of a solid solution is a spontaneous decomposition due to energetic advantages, i.e. the gain of free enthalpy.

$Ti_{1-X}Al_XN$ can be subject to spinodal decomposition at elevated temperatures. Annealing of $Ti_{1-X}Al_XN$ at 900 °C leads to the precipitation of fcc AlN and fcc TiN from the metastable fcc $Ti_{1-X}Al_XN$:

$$\text{fcc-TiAlN} \rightarrow \text{fcc-TiN} + \text{fcc-AlN}$$

At temperatures of 1100 to 1250 °C cubic AlN transforms into hexagonal AlN:

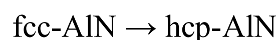

$$\text{fcc-AlN} \rightarrow \text{hcp-AlN}$$

Thus, the entire transformation of $Ti_{1-X}Al_XN$ from the metastable cubic phase to the equilibrium two-phase structure can be written as:

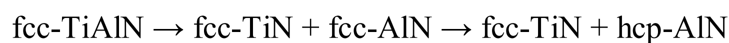

$$\text{fcc-TiAlN} \rightarrow \text{fcc-TiN} + \text{fcc-AlN} \rightarrow \text{fcc-TiN} + \text{hcp-AlN}$$

For the formation of hexagonal AlN, a huge amount of energy is needed to overcome the nucleation barrier, which is a result of the larger atomic volume of the wurtzite phase and the necessarily forming incoherent interfaces with the cubic TiN. As the formation of cubic AlN is associated with a lower effort of energy, the intermediate step of the formation of cubic AlN can be observed [47].

5.2 Mechanical Properties

In the following paragraphs, mechanical properties of $Ti_{1-X}Al_XN$ such as hardness and Young's Modulus are considered. The hardness of $Ti_{1-X}Al_XN$ increases with increasing Al content (fig. 5.4a and b). The maximum hardness and as well Young's modulus (fig. 5.4b) are observed in coatings with Al/Ti ratios of about 0.5 to 0.6. Beyond this value both hardness and Young's modulus decrease drastically due to the formation of the hexagonal wurtzite phase. According to Zhou *et al.* [39], the increase in hardness can be explained on the basis of bonding characteristics. With the addition of Al the interatomic distance decreases (compare the consideration of the lattice parameter in section 5.1 and fig. 5.4a). This leads to an increasing bulk modulus and consequently to a distinct increase in hardness [36].

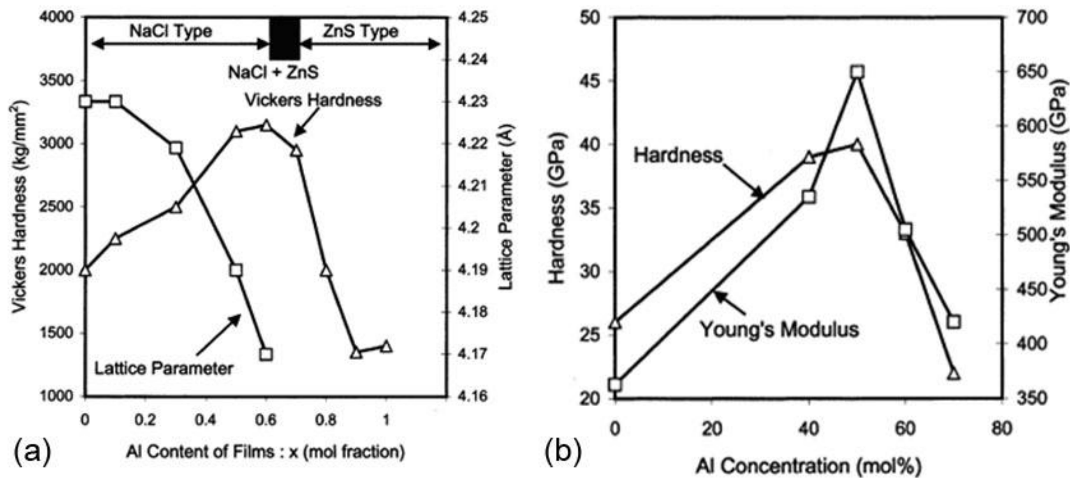

Fig. 5.4: (a) Vickers hardness and lattice parameter of $Ti_{1-X}Al_XN$ films as a function of the Al content, (b) hardness and Young's modulus of $Ti_{1-X}Al_XN$ films as a function of the Al content [36].

Mayrhofer *et al.* investigated the development of the hardness during spinodal decomposition and observed a distinct increase of hardness in the temperature range between 600 and 1000 °C. This increase in hardness is related to the formation of the coherent cubic AlN intermediate phase. At temperatures above 1000 °C the hardness decreases, due to the precipitation of the incoherent hexagonal AlN equilibrium phase [48].

5.3 Tribological Properties

The wear resistance of $Ti_{1-X}Al_XN$ is basically determined by the Ti/Al ratio, the coating hardness and its microstructure. The target composition, substrate bias and nitrogen partial pressure are the most important parameters to influence the tribological properties [49].

The composition of the target more or less determines the coating composition and therefore the properties of the film. According to Lin *et al.* [49] coatings prepared with a 50/50 Ti/Al atomic ratio target show better wear resistance than coatings produced by a 72/28 Ti/Al target [36, 49].

Both coating composition and microstructure are influenced by the substrate bias. In fact, the Al content has been reported to decrease with increasing bias voltage for arc-evaporated coatings. Hence, the wear resistance can, to a certain extent, provided that the necessary coating density is maintained, be improved by lowering the bias voltage. According to their different ionization probability, the degree of ionization is higher for Ti vapor than for Al vapor. Therefore, preferably Ti ions are attracted to the biased substrate. Furthermore, the coating composition is influenced by back scattering effects. Due to their lower atomic mass, the Al atoms have a higher back scattering probability than the heavier Ti atoms [36, 49].

The nitrogen partial pressure affects the Al content and the microstructure of the coating, as well as the coating adhesion and the growth rate of sputter deposited coatings. In sputtering, the deposition rate, e.g. decreases with increasing nitrogen partial pressure due to target poisoning effects and collisions and scattering of the particles (compare also chapter 7) [36, 50, 51].

$Ti_{1-X}Al_XN$ exhibits high hot hardness which is favorable for the resistance against abrasive wear. As already mentioned above, $Ti_{1-X}Al_XN$ shows excellent high temperature stability due to the formation of a protecting Al_2O_3 surface layer which inhibits diffusion of oxygen into the coating. Furthermore, it exhibits low thermal conductivity and prevents direct contact of the $Ti_{1-X}Al_XN$ coating and the wearing material. Therefore, the Al_2O_3 layer also reduces adhesive wear [36, 52].

In fig. 5.5a and b the tool life and maximum flank wear of PVD TiN, TiCN and TiAlN are compared, proving the excellent wear performance of $Ti_{1-X}Al_XN$ coated tools [53].

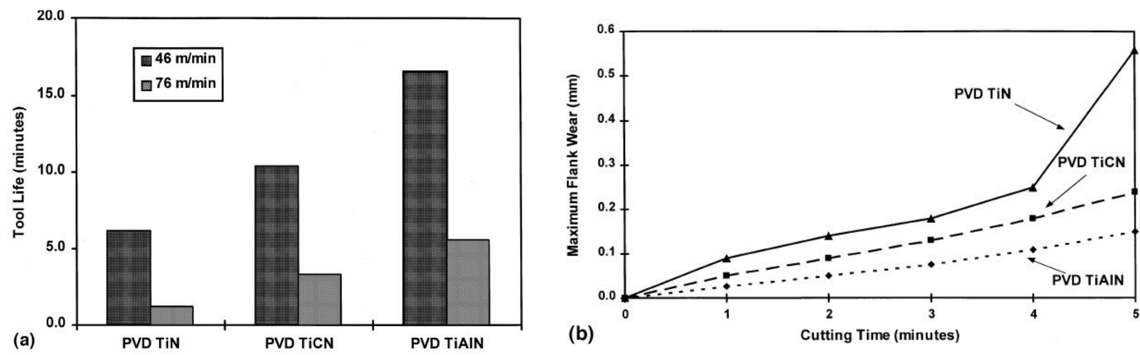

Fig. 5.5: (a) Comparison of the tool life between PVD TiN, TiCN and TiAlN coated inserts in turning of Inconel 718, (b) comparison of the maximum flank wear over time between PVD TiN, TiCN and TiAlN [53].

6 Experimental Details

6.1 Targets

In sputter deposition, there are different possibilities to produce multicomponent thin films. One is to use different pure element targets, another one is to use compound targets. Alloy targets can be made by various processing techniques, such as casting and powder metallurgical techniques like sintering and hot pressing. Other possibilities are studded targets or targets made of the first component with several drilled holes filled with another element. In the latter case of so-called mosaic targets, the film composition can be varied through the number and position of the holes [36].

Two different types of TiAl targets were used for the present diploma thesis: powder metallurgical (PM) targets (fig. 6.1a) produced by PLANSEE Composite Materials in Lechbruck, Germany, and ingot metallurgically produced targets with filled holes, also referred to as CemeCon type mosaic targets (fig. 6.2b) produced by CemeCon in Würselen, Germany.

Both types of targets are 10 mm thick, 500 mm high and 88 mm broad. In case of the mosaic targets, the target matrix material is Ti and the holes are filled with Al inserts. This compound is approximately 6 mm thick and bonded to an approximately 4 mm thick copper back plate. The mosaic targets are of CemeCon type TiAl48GM, which means that they have 48 Al filled holes which are positioned in the middle of the erosion track (fig. 6.1b). For films deposited with these targets, a metal composition of approximately 60 % Al and 40 % Ti can be expected. The PM targets (fig. 6.1a) contain 60 % Al and 40 % Ti and consist of two phases, i.e. an Al matrix with Ti grain embedded. The usable sputter area is 10 mm thick.

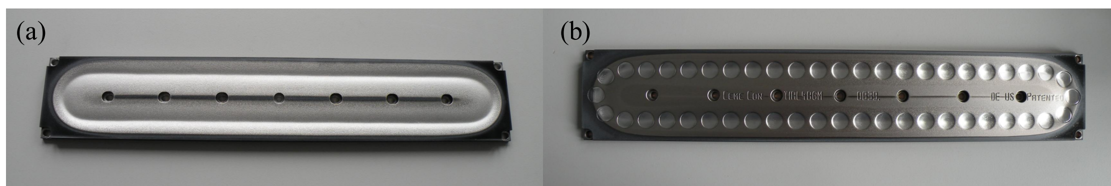

Fig. 6.1: (a) PLANSEE PM target with erosion track, (b) CemeCon type mosaic target TiAl48GM.

6.2 Substrates

The substrates coated within the present work were high speed steel (HSS) disks of type S290 fabricated by Böhler Edelstahl in Kapfenberg, Austria. This powder metallurgically produced HSS is mainly used for high-performance metal cutting. The S290 exhibits excellent hot

hardness and wear resistance as well as very high hardness (up to 70 HRC). Due to its chemical composition it can be classified as HS14-2.5-5-11 (AISI M2).

Additionally, silicon samples with the dimensions 7x21x0.38 mm were coated. The coated silicon samples were used to determine the internal stresses of the coating, while for all other investigations the coated HSS substrates were used [54, 55].

6.3 Coating Deposition

All coatings for the present work have been deposited by reactive unbalanced magnetron sputtering with an industrial-scale sputtering device of the type CemeCon CC800® /9MLT (fig. 6.2) at the University of Leoben. The CC800® /9MLT is equipped with four bipolar pulsed DC magnetrons of the size 500x88 mm. The assembly of one pair of cathodes can be seen on the right side; the second pair is assembled equally on the opposite side.

Fig. 6.2: Picture of the industrial scale sputtering device CemeCon CC800® /9MLT at the University of Leoben.

Prior to deposition, the substrates were ultrasonically cleaned in acetone and ethanol for ten minutes each. Then they were mounted on the substrate carousel of the sputtering plant. As this sputtering plant is of industrial scale, all deposition processes recipes can be programmed and run automatically.

All coating deposition recipes used for this work were built up very similarly. After evacuating the chamber to a base pressure of ≤ 4 mPa (= $4 \cdot 10^{-5}$ mbar), the substrates were cleaned through a heating step and subsequently by Ar^+ ion etching. There, the substrate is bombarded by the Ar^+ ions from the ignited plasma, where the substrate carousel acts as the anode. After substrate ion etching, the actual deposition process was started.

Using the PM targets, all depositions were carried out with a unipolarily pulsed bias voltage of -40 V at a pulse frequency of 350 kHz and a reversal time of 1000 ns. The deposition time was set to 1.5 h at deposition temperatures of approximately 525 °C to 550 °C. The flow of the argon working gas was 200 sccm. The target power and nitrogen partial pressure were varied to find the most efficient parameters. In tab. 6.1, the values for the various deposition recipes are summarized. As the flow of the argon working gas was constant, the total pressure variation was only caused by the changing nitrogen flow.

Tab. 6.1: Varied deposition parameters for PM targets.

Process	Cathode power [kW]	Total pressure [mPa]
R473	4,5	560
R474	4,5	570
R475	4,5	550
R476	6,0	560
R477	6,0	540
R478	6,0	580
R479	7,0	580
R480	7,0	600
R481	7,0	620

A standard process was available for the CemeCon type mosaic targets; the unipolarily pulsed bias voltage was set to -50 V, the pulse frequency 350 kHz and the reversal time 1000 ns. The cathode power was 7 kW and the total pressure 580 mPa, where the flow of the argon working gas was 230 sccm. The deposition temperature was also approximately 525 °C to 550 °C. A deposition time of 2.5 h was chosen.

6.4 Simulation of sputter process

The sputtering yield as well as the energy of film forming neutrals for a given target and specific kinetic parameters can be calculated using a statistic program such as SRIM (Stopping and Range of Ions in Matter) [56].

The values obtained by SRIM within this thesis represent number and energy of the sputtered atoms at the time when they leave the target surface. During their travel to the substrate, they may lose energy due to collision processes. This energy loss is mainly influenced by the total pressure, which determines the mean free path, and the so called energy transfer coefficient ε, given as:

$$\varepsilon = \frac{4 \cdot m_t \cdot m_i}{(m_t + m_i)^2} \quad (6.1)$$

There, m_t denotes the mass of the target atom and m_i the mass of the ion. Thus, the energy transfer coefficient reaches a maximum for a minimal mass difference between the ions and the target atoms [57]. In tab. 6.2, the atomic masses of the target atoms as well as the gas atoms are summarized.

Tab. 6.2: Atomic masses of target atoms and process gas ions.

Element	Atomic mass
Al	26.98
Ti	47.87
N	14.00
Ar	39.95

6.5 Coating Characterization

6.5.1 Coating Thickness

The coating thickness was determined using the ball crater technique, which is schematically shown in fig. 6.3.

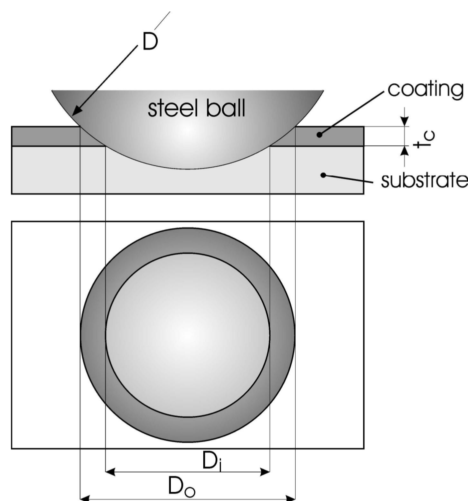

Fig. 6.3: Ball crater technique [17].

This technique is very common due to the quick and easy application. A steel ball covered by a diamond suspension is used to grind a crater into the coating by rotational movement. The inner (D_i) and outer (D_o) diameters of the resulting spherical calotte are then measured using an optical Reichert-Jung microscope of type Polyvar Met with an attached CCD camera and the analySIS® software of Soft Imaging System.

The coating thickness can be calculated by using the following equation:

$$t_c = \frac{D_0^2 - D_i^2}{4 \cdot D} \tag{6.2}$$

Here, D denotes the diameter of the steel ball [58].

6.5.2 Chemical Composition

Besides the reactive elements added, the actual elemental composition of the coatings often differs from the target composition. Energy-dispersive x-ray emission spectroscopy (EDX) utilizing an Oxford Instruments INCA extension in a Zeiss EVO 50 scanning electron microscope (SEM) was used to determine the coating composition. Four specimens were investigated, i.e. those three deposited with the PM targets at 7.0 kW (R479 – R481) and the reference coating deposited with the mosaic targets (R482).

6.5.3 Microstructure

X-ray diffraction (XRD) is a non-destructive characterization technique for the determination of the crystalline structure of solids. With this technique, chemical and phase analyses can be done as well as stress analyses. Furthermore, it is possible to determine e.g. the grain size and the coating texture.

In the present work, all coatings were analyzed using a Siemens D500 diffractometer in Bragg-Brentano as well as in grazing incidence configuration. In fig. 6.4, a schematic of the Bragg-Brentano configuration is shown. A range of the incident angle θ has to be selected. The sample is irradiated with an X-ray incident at an angle θ to the surface of the sample and the diffracted beam intensity is detected at an angle 2θ with respect to the incident beam. As with this method also peaks of the bulk material are obtained, the samples are also investigated in grazing incidence mode. There, the incident angle θ is adjusted to a constant small value and only the diffraction angle 2θ passes through the selected angle range. Thus, only information of the surface-near area (i.e. the coating if the thickness is sufficient) is obtained and the resulting patterns are easier to evaluate than those obtained in Bragg-Brentano mode.

For the investigation within the present work, an incident angle of 2° was chosen [59]. The parameters used are presented in tab. 6.3.

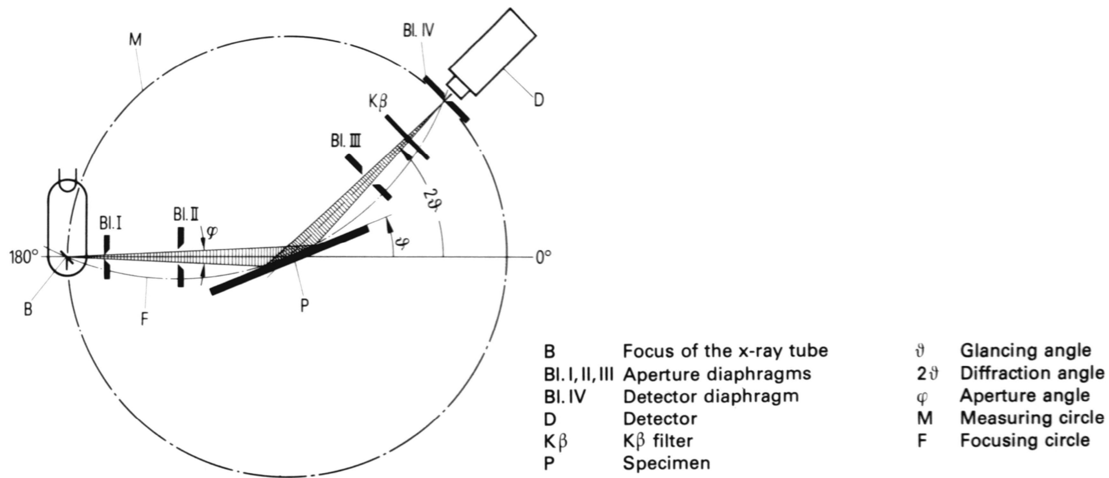

Fig. 6.4: XRD beam path in Bragg-Brentano configuration [60].

Tab. 6.3: Parameters used for the XRD investigations.

Voltage [kV]	Tube current [mA]	Step time [s]	Step size [°]	Angle range 2θ [°]
40	25	1.2	0.02	25-85

The incident X-ray is only reflected if the Bragg condition is fulfilled:

$$n \cdot \lambda = 2 \cdot d \cdot \sin\theta \tag{6.3}$$

Here, n is the order of reflection, λ the X-ray wavelength and d the lattice spacing. In XRD investigations, plots of the intensity of the diffracted beam versus the diffraction angle are obtained.

Grain size and strain can be determined by the analysis of the peak broadening. The Pseudo-Voigt function, which is a linear combination of a Cauchy (Lorentzian) f_{Cauchy} and a Gaussian function $f_{Gaussian}$, is fitted to the X-ray patterns by:

$$f(x) = f_0 + A \cdot \left[\eta \cdot f_{Cauchy} + (1-\eta) \cdot f_{Gaussian}\right] \tag{6.4}$$

Here, f_0 denotes the mean background level, A the peak area and η the Cauchy component. The Cauchy component of the measured profile is induced solely due to the crystallite size or more precisely, the size of coherently diffracting domains, hereafter called domain size. The Gaussian component arises from the strain [61].

To get information about a preferred orientation of the coating, the texture coefficient TC was determined using the modified Harris formula. The texture coefficient is given by:

$$TC = \frac{\frac{I_{m(hkl)}}{I_{0(hkl)}}}{\frac{1}{n}\sum_{i=1}^{n}\frac{I_{m(hkl)}}{I_{0(hkl)}}} \qquad (6.5)$$

$I_{m(hkl)}$ is the measured intensity of the reflection from the (hkl) plane and $I_{0(hkl)}$ is the corresponding intensity of an untextured reference powder sample (cubic AlN, JCPDS 00-025-1495, cubic TiN, JCPDS 00-038-1420). n is the number of analyzed peaks. The orientation with the highest texture coefficient is the preferred one [62, 63, 64, 65].

6.5.4 Film Adhesion

Film adhesion was determined by Rockwell indentation adhesion tests. A conventional Mitutoyo Rockwell C hardness tester, type DT-10 was used. The indentation causes a massive plastic deformation in the coated surface. This leads to damage of the coating in the surrounding of the indent and thus to the formation of a crack network or, in case of insufficient film adhesion, to coating delamination. Coating adhesion can be classified to HF1 – HF6 using an optical Reichert-Jung Polyvar Met microscope and comparing the coating damage with fig. 6.5. HF5 and HF6 indicate that the film adhesion is insufficient [66].

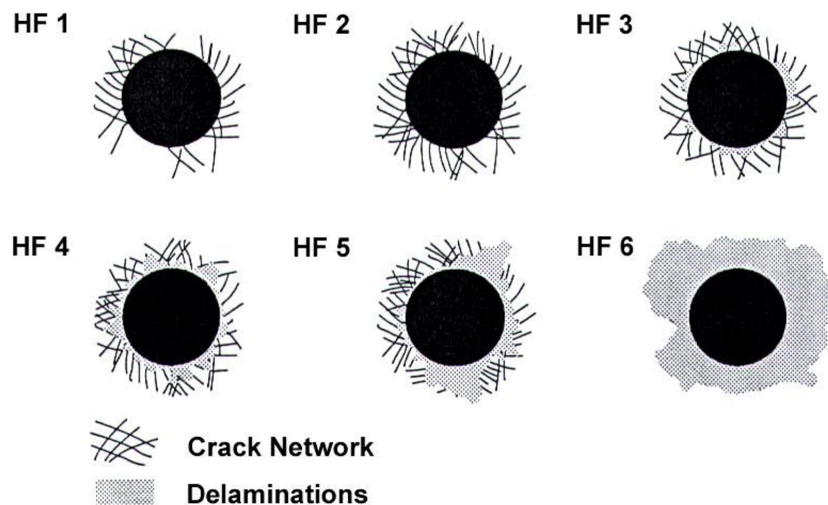

Fig. 6.5: Classes of film adhesion in the Rockwell C test [66].

6.5.5 Hardness and Young's Modulus

For determination of hardness and Young's modulus of thin films, it is important to ensure that only the properties of the film are measured and any influence of the substrate can be excluded. Hence, the indentation depth should be less than 10 % of the film thickness. To fulfill this demand, all hardness measurements were carried out by a UMIS Nanoindenter (Ultra Micro Indentation System) from Fischer-Cripps Laboratories [67]. The system is equipped with a Berkovich indenter, which is a three-sided pyramid with a face angle of 65.3°, made of diamond [68].

The classical definition of hardness is the ratio of the peak load F to the projected contact area A. With nanoindentation, load-displacement curves (fig. 6.6) are measured.

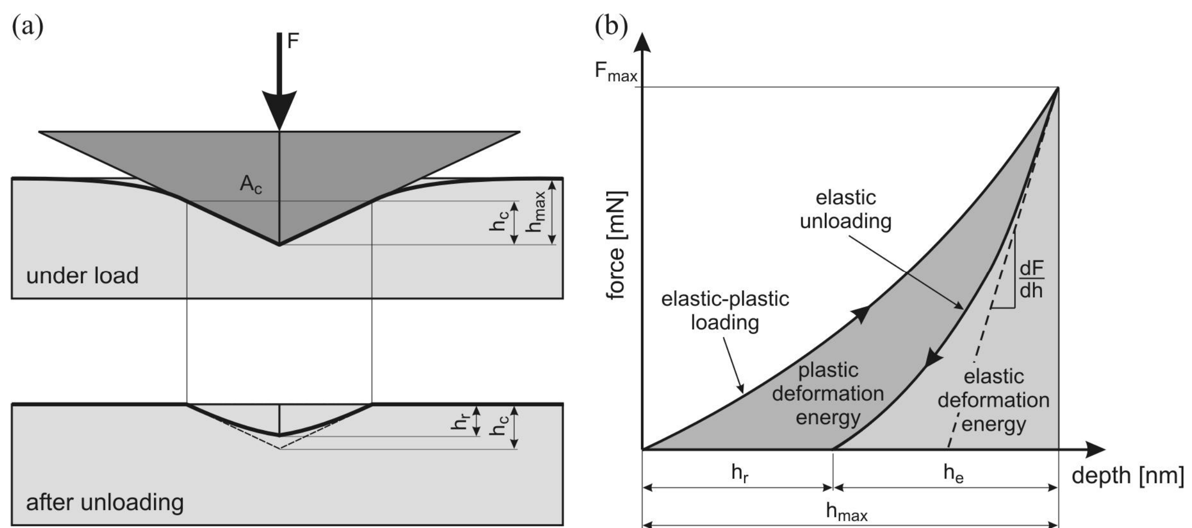

Fig. 6.6: (a) cross section of an indentation at full load and full unload for elastic-plastic conditions, (b) load-displacement curve [68].

As in reality the geometry of the tip is not ideal but always somewhat rounded, this is taken into account by using an area function in combination with the indentation depth to determine the true contact area.

Within this thesis, a plateau test was carried out with a maximum force of 40 mN and a minimal force of 2 mN with an increment of 2 mN. To exclude the potential influence of surface irregularities, a calotte was ground into the surface (compare subsection 6.5.1) with an OP-S (oxide particle) suspension and just for a few seconds to skim the surface and not too much of the coating thickness. The plateau test was performed in the central area of the calotte. With the obtained data, the Young's modulus and the hardness were determined.

6.5.6 Coating Stress

To determine the residual stresses, which virtually all PVD coatings exhibit, silicon substrates were also mounted on the carousel during deposition and subsequently examined with the so called wafer curvature method. If a relatively thin substrate is coated on one side only, the residual stresses will cause the whole substrate-coating composite to bend (fig. 6.7).

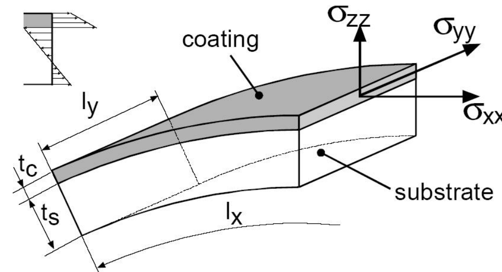

Fig. 6.7: Bended substrate-coating composite [17].

The measurements of the curvature were carried out on a device called “Mutti 2000”, constructed by Winkler [69]. A schematic is shown in fig. 6.8. There, the surface of the coated silicon substrate is irradiated by two parallel laser beams with the defined distance d_0. The laser beams are first reflected by the substrate surface and hit a mirror in the defined distance h_1. There, they are again reflected and finally they hit the measuring plate in the defined distance h_2, where their distance d_1 can be measured.

With this information, the bending radius r of the coated sample can be determined as follows:

$$r = \frac{2 \cdot (h_1 + h_2) \cdot d_0}{d_0 - d_1} \tag{6.6}$$

Subsequently the internal stress can be determined with the help of the modified Stoney equation:

$$\sigma = \frac{E_s}{1 - \nu_s} \cdot \frac{t_s^2}{6 \cdot t_c} \cdot \left(\frac{1}{r} - \frac{1}{r_0} \right) \tag{6.7}$$

There, E_s denotes the Young’s modulus and ν_s the Poisson’s ratio of the substrate, t_s and t_c are the substrate and the coating thickness, respectively, and r_0 is the bending radius of the uncoated sample [58, 69].

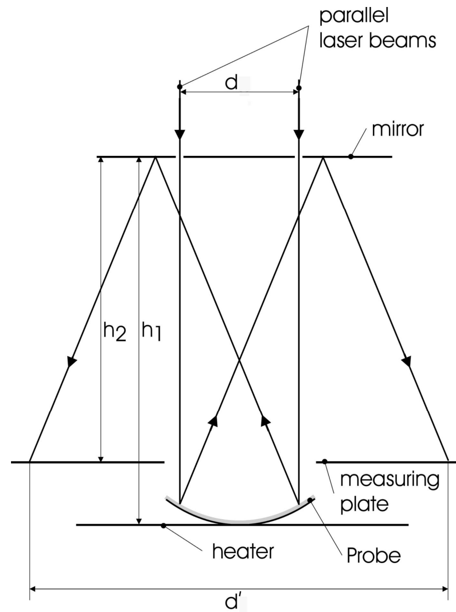

Fig. 6.8: Schematic of the measurement setup of Mutti 2000 [17].

6.5.7 Tribological Properties

The tribological investigations were carried out by ball-on-disk tests [54] using a high temperature tribometer of CSM Instruments. All samples were investigated at room temperature; the humidity was 27 ± 1 %. A wear track radius of 7 mm, a sliding distance of 300 m and a normal load of 5 N were chosen. The linear speed was 10 cm/s. The 6 mm diameter ball was made of Al_2O_3.

Following the ball-on-disk test the resulting wear tracks were examined by white-light optical profilometry. With this method it is possible to characterize the surface topography and thus calculate, e.g. the wear coefficient K as follows [28]:

$$K = \frac{V_{ges}}{(F \cdot s)} \tag{6.8}$$

There, F is the normal load, s the sliding distance and V_{ges} is given as:

$$V_{ges} = V \cdot \frac{(2 \cdot r \cdot \pi)}{l} \tag{6.9}$$

V denotes the wear volume which is determined by optical profilometry, r the radius of the wear track and l the length of the section for which the negative wear volume is determined.

The measurements were carried out on a Veeco Wyko NT1000 white light interferometer in VSI-mode (Vertical Scanning Interferometry). The used software was Wyko® Vision32.

7 Results and Discussion

7.1 Cathode Power and Nitrogen Partial Pressure Variation

As with the utilized sputter device to date only mosaic targets have been used, first of all a deposition process for the PM targets had to be developed by optimization of sputter cathode power and nitrogen partial pressure. As already mentioned in section 6.3, in the CemeCon sputter system used the nitrogen fraction in the process gas is added to the constant argon flow; thus the controlled total pressure is directly related to the nitrogen partial pressure. To evaluate the target performance, for the first coating deposited a total pressure of 560 mPa and a cathode power of 4.5 kW were chosen. Subsequently, the evolution of the cathode voltage versus time (fig. 7.1) was examined for all four cathodes used (termed as cathodes 1-4 in the subsequent figures). According to fig. 7.1, a slight increase of the cathode voltage during deposition can be observed. Such an increase of the cathode voltage indicates a possible poisoning of the targets. This means that the target surface changes from metallic state to poisoned (i.e. nitride) state caused by the formation of a compound on the target surface [19, 70].

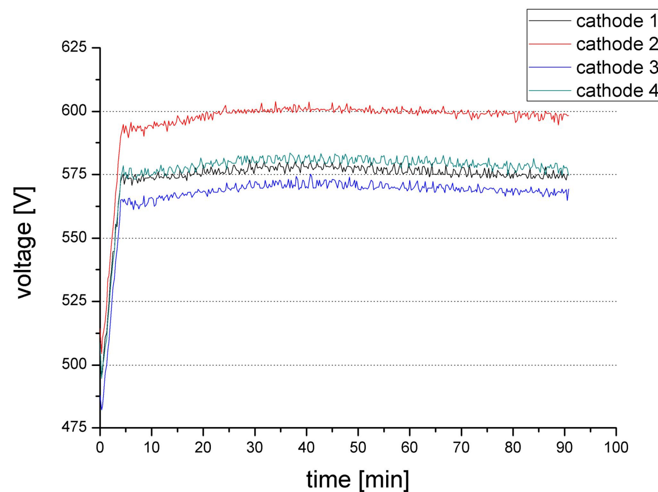

Fig. 7.1: Cathode voltage evolution for PM TiAl targets: process R473 (cathode power: 4.5 kW, total pressure: 560 mPa).

In target poisoning, the cathode voltage already changes due to minor modifications of the target surface condition. Depla *et al.* [19] stated that the poisoning mechanism is based on reactive gas ion implantation during sputtering. There are three possible pathways for these implanted ions: (*i*) chemical reaction between the implanted ions and the target material, (*ii*) the implanted nitrogen remains in the target as non-reacted atoms, or (*iii*) the nitrogen atoms recombine in the target and diffuse from there. The compound formation results in a decrease

of the target erosion rate. However, the cathode voltage depends not only on the target surface condition but also on the plasma condition, which also changes during poisoning [19, 70].

In fig. 7.2 a typical hysteresis between poisoning and de-poisoning of a silicon target sputtered in an argon/nitrogen discharge, as obtained by Depla *et al.* [70], is shown. At a nitrogen mole fraction of x = 0.28 in the process gas a sudden increase of the cathode voltage with increasing nitrogen content can be observed; this indicates a change in the surface condition and therefore the transition from metallic to poisoned state.

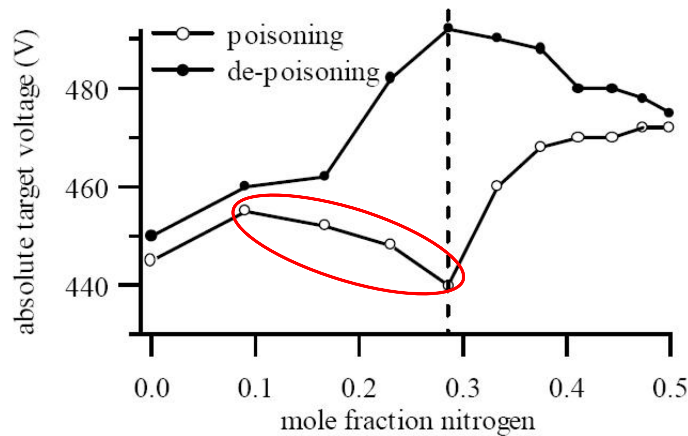

Fig. 7.2: Sputtering of a silicon target in an argon/nitrogen discharge: Hysteresis behavior of the cathode voltage as a function of the nitrogen mole fraction. The marked area denotes where the deposition processes investigated within this thesis are located in such a hysteresis [70, modified].

To find out in which area of such a hysteresis the deposition processes investigated within this thesis are located, two further depositions were done with the same cathode power but different total pressures; one with 570 mPa and one with 550 mPa. This corresponds to a reduction of the nitrogen partial pressure, as explained in section 6.3. These experiments show that with less nitrogen the increase of the cathode voltage during deposition is much more pronounced, while more nitrogen results in a less marked increase. Additionally, the absolute cathode voltage decreases with increasing nitrogen partial pressure. This reveals that the depositions carried out are somewhere in the marked “metallic” area of the hysteresis shown in fig. 7.2 and that therefore poisoning does not play a role. According to Depla *et al.* [70], this decrease of the absolute cathode voltage with increasing pressure is due to the reduced plasma impedance.

In the second deposition series, the cathode power was increased to 6.0 kW and the total pressures were varied between 540 mPa and 580 mPa. Again, a similar phenomenon as in the first series can be observed: With a total pressure of 560 mPa a slight increase of the cathode voltage was found (fig. 7.3b). At 540 mPa (fig. 7.3a), the increase is much more pronounced, while with 580 mPa (7.3c) the process runs more stable, i.e. with a lower number of arcs,

which are represented by the pronounced negative spikes in fig. 7.3a. At 540 mPa, in total 2091 arcs were detected during the 90 min. sputter process, whereas at 560 and 580 mPa only 830 and 316 arcs, respectively, were counted.

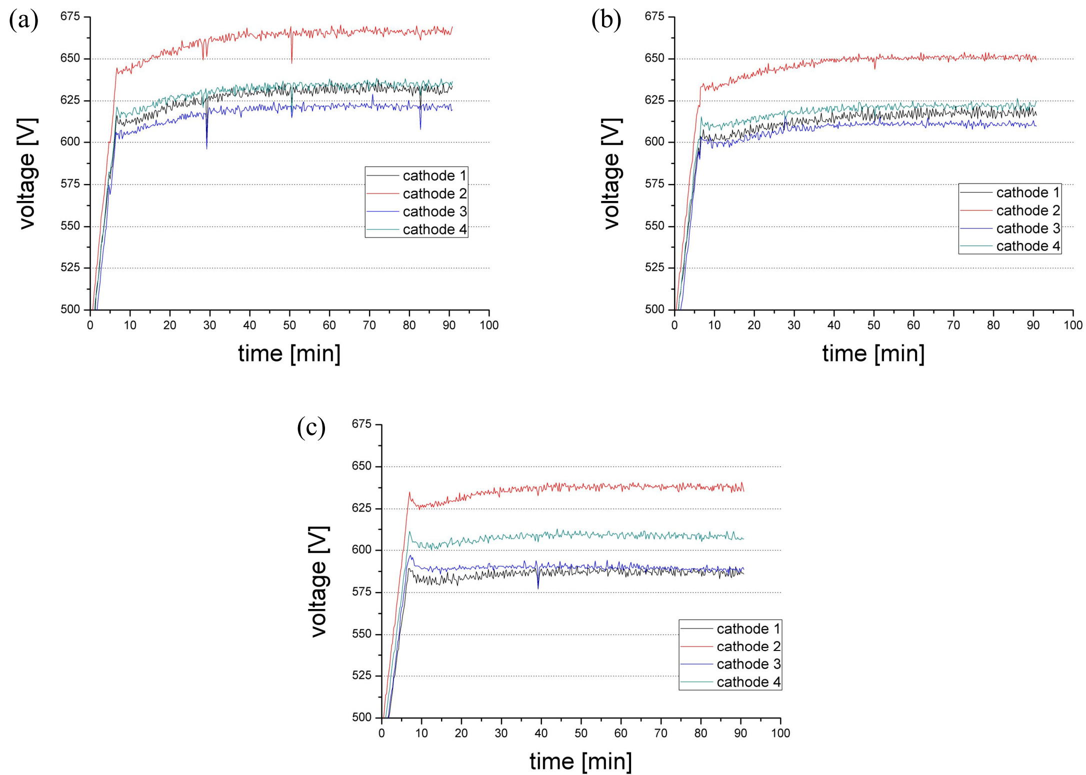

Fig. 7.3: Cathode voltage evolution for PM TiAl targets: Processes (a) R477, cathode power: 6.0 kW, total pressure: 540 mPa, (b) R476, 6.0 kW, 560 mPa, (c) R478, 6.0 kW, 580 mPa.

Based on this information, the cathode power was further increased to 7.0 kW in the third series. At this power level, a slight increase of cathode voltage can still be observed for a total pressure of 580 mPa. Also some arcs can be identified. At 600 mPa, the process is more stable and at 620 mPa there are also no arcs anymore to be detected. In fig. 7.4a, the cathode voltage versus time development of process R481 done at a cathode power of 7.0 kW and a total pressure of 620 mPa is shown. This appears to be the most stable and efficient process, which is with respect to the arcing behavior and the constant cathode voltage comparable to the standard CemeCon process (fig. 7.4b) using the mosaic targets.

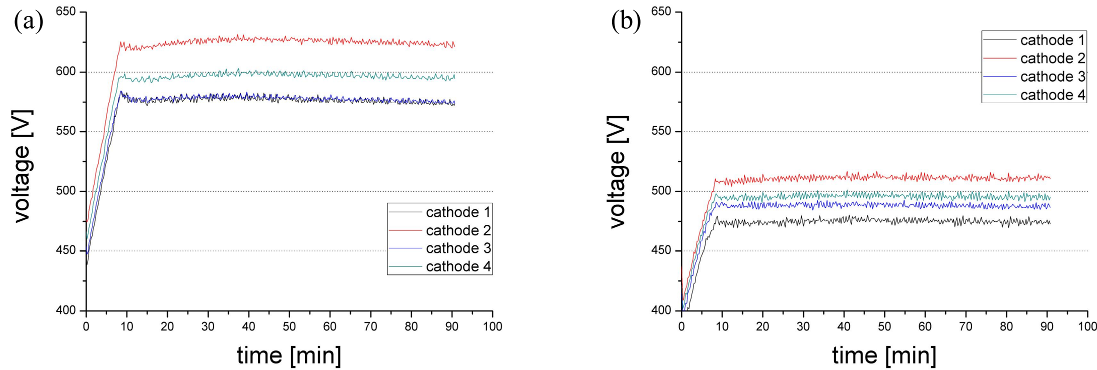

Fig. 7.4: Cathode voltage evolution for (a) PM TiAl targets: Process R481, cathode power: 7.0 kW, total pressure: 620 mPa and (b) CemeCon type mosaic TiAl targets: Process R482, 7.0 kW, 580 mPa.

7.2 Sputter Behavior

7.2.1 Coating Thickness and Deposition Rate

In fig. 7.5 the abrasion crater (coating R480 deposited from the PM targets, cathode power: 7.0 kW, total pressure: 600 mPa) caused by spherical abrasion (compare subsection 6.5.1) is shown as a representative example. Such a calotte is examined with an optical microscope to determine the coating thickness.

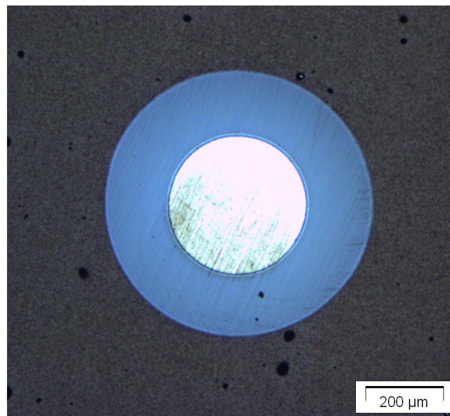

Fig. 7.5: Abrasion crater of coating R480 deposited from the PM targets, cathode power: 7.0 kW, total pressure: 600 mPa.

Tab. 7.1 shows the thicknesses and deposition rates of the different coatings, where the latter were calculated from the coating thickness and the corresponding deposition time. The evolution of the deposition rate versus total pressure is additionally shown in fig. 7.6. Basically, it can be seen that at constant cathode power the deposition rate slightly decreases with increasing total pressure. In general, such a decrease in deposition rate at high total pressures, which

corresponds to an increased nitrogen partial pressure in the used sputtering system (compare section 6.3), can be related to target poisoning as well as an increasing number of collisions and scattering effects of the atoms and molecules. Since, according to section 7.1, significant poisoning of the targets can be excluded, the observed decrease in deposition rate can mainly be attributed to more collisions and scattering of sputtered atoms, which lead to a reduction of the number of film-forming species arriving at the substrate as well as to a decrease of their kinetic energy [50].

Tab. 7.1: Summary of coating thicknesses and deposition rates of the coatings investigated within this work. Processes R473 – R481 have been done with PM targets, R482 is the standard CemeCon process with mosaic targets.

Process	Cathode power	Total pressure	Coating thickness	Deposition rate
	[kW]	[mPa]	[µm]	[nm/min]
R473	4.5	560	2,77	31
R474		570	2,55	28
R475		550	2,65	29
R476	6.0	560	3,44	38
R477		540	3,80	42
R478		580	3,21	36
R479	7.0	580	3,62	40
R480		600	3,34	37
R481		620	3,21	36
R482	7.0	580	3,69	25

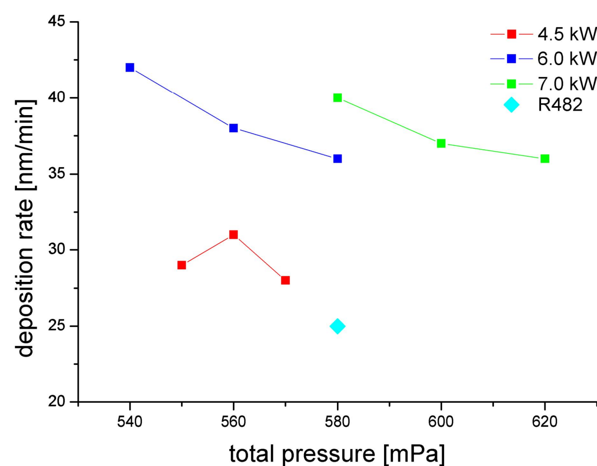

Fig. 7.6: Evolution of the deposition rate versus total pressure at different cathode powers for PM targets and for process R482 using mosaic targets.

Besides, it is obvious that the deposition rate determined for the process R482, which is the process based on the CemeCon mosaic targets, is significantly lower than the rates obtained for the other processes with the PM targets. Process R479, which was done at the same total pressure, shows a ~ 60 % higher deposition rate. Even the deposition rate of process R481, which was run at an increased total pressure of 620 mPa, was 44 % higher. These results strongly suggest that the difference in deposition rate can be related to the different targets and, consequently, to their different sputter behavior (compare section 6.4 and subsection 7.2.2), since the collisions and scattering effects in the transport phase at the same total pressure are comparable.

The number and energy of film-forming neutrals sputtered from the target depends not only on the sputtering yield, but also on the energy and number of inert gas ions impinging on the target surface [57], which again depend on parameters like cathode voltage and current, the total pressure as well as the target material itself. For example, a higher cathode current indicates that more ions hit the target surface, which should therefore result in a higher sputtering rate.

On the other hand, the ion energy E_i and the ion flux density J_i at the substrate can be controlled by the substrate bias voltage. A higher bias voltage means that more ions are attracted to the substrate, reaching it at higher kinetic energy, which results in a higher substrate current. However, with increasing bias voltage re-sputtering may play a certain role [57].

Furthermore, the ion energy and the flux density at the substrate are influenced by other parameters such as, for example, the total pressure but also the cathode current [57, 71]. This can also be observed in the experiments performed for this thesis, where the influence of the cathode current is very distinct, while the increasing total pressure affects the substrate current negligibly. In fig. 7.7, the cathode currents as well as the substrate currents of three different processes are shown. Comparing the two processes R473 (fig. 7.7a) deposited at a cathode power of 4.5 kW and a total pressure of 560 mPa and R481 (fig. 7.7b) deposited at 7.0 kW and 620 mPa, both carried out with PM targets, it is apparent that with increasing cathode power and consequently increasing cathode current also the substrate current increases. By comparing process R481 with R482 (fig 7.7c), which was carried out with mosaic targets at 7.0 kW and 580 mPa, it is obvious that the cathode as well as the substrate current of R482 is noticeable higher. The higher substrate current can in part be explained by the higher bias voltage of process R482, but should also be related to the higher cathode current. There, the higher cathode current can be attributed to the different target materials and their properties, which will result in potentially different plasma conditions. The higher cathode current (~ 17 %) of process R482 should be connected to a higher sputtering rate, but as a result of the higher bias voltage (~ 25 %) re-sputtering might also play a role reducing the deposition rate. Thus, these two effects might at least in part compensate each other.

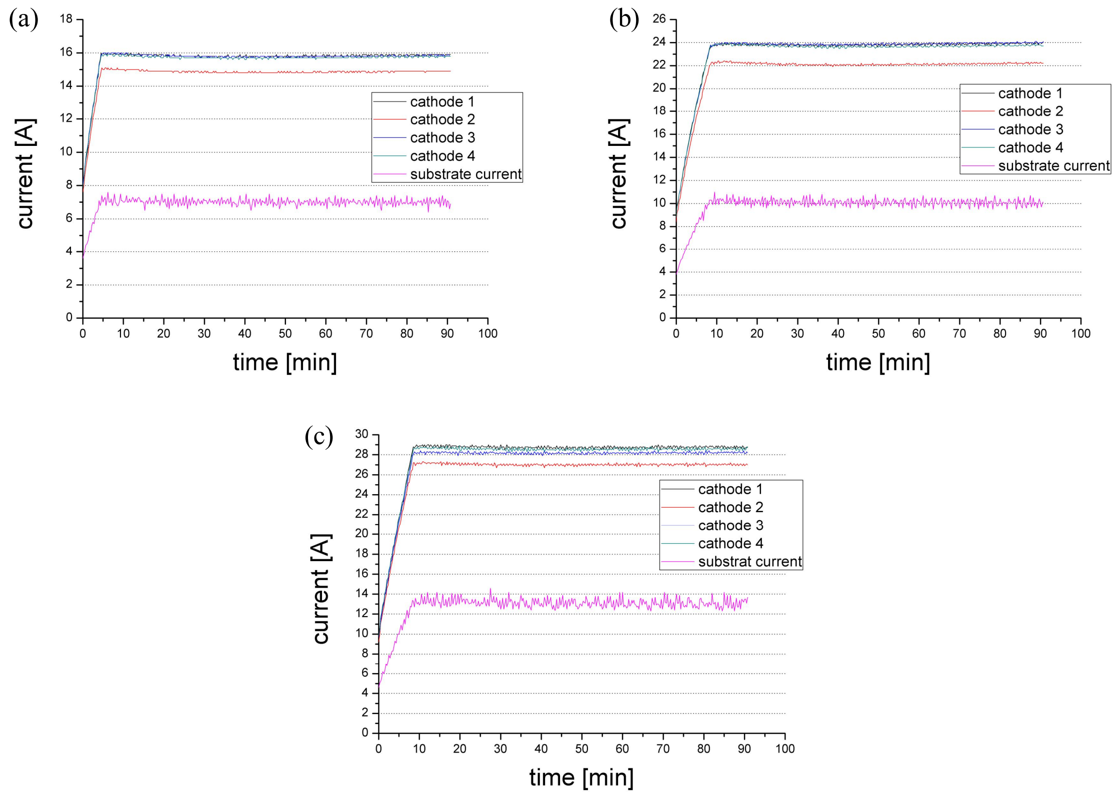

Fig. 7.7: Cathode and substrate current evolution for (a) PM TiAl targets: Process R473, 4.5 kW, 560 mPa, -40 V bias, (b) PM TiAl targets: Process R481, 7.0 kW, 620 mPa, -40 V bias, (c) mosaic TiAl targets: Process R482, 7.0 kW, 580 mPa, -50 V bias.

7.2.2 SRIM Simulation

By applying the SRIM software package (compare section 6.4), the sputtering yields were calculated as a function of their kinetic energy which corresponds to the difference of cathode voltage and plasma potential [57] for different target materials and process gases. The obtained results are shown in fig. 7.8. There, the black and the red curves represent the sputtering yields of single-phase aluminum and titanium targets, respectively, bombarded by nitrogen ions, while the turquoise line stands for titanium and the blue line for aluminum, both subjected to bombardment with argon ions. It can clearly be seen, that the combination of aluminum target and nitrogen ions results in the highest sputtering yield while nitrogen ions bombarding titanium the lowest ones were obtained. This is related to the highest energy transfer coefficient as explained in section 6.4.

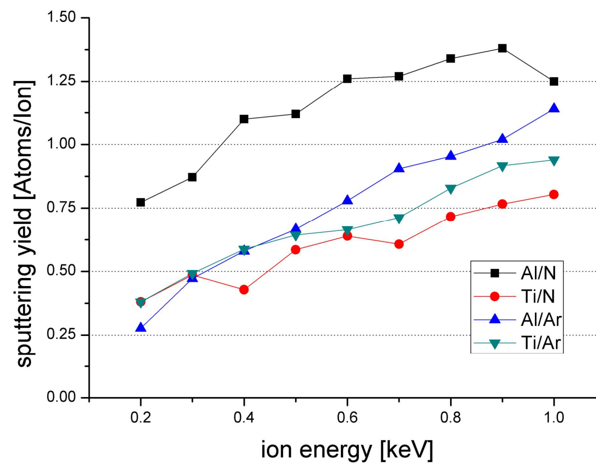

Fig. 7.8: Sputtering yields calculated by SRIM as a function of the cathode voltage for different target materials bombarded by argon or nitrogen ions of given kinetic energy.

The argon to nitrogen pressure ratio for the depositions done with the PM targets was varied between 70:30 and 60:40. In case of the mosaic targets it was 60:40. Consequently, the sputtering yields shown in fig. 7.9 are averaged for an argon/nitrogen pressure ratio of 60:40. The cathode voltage for the PM targets was in average -600 V during negative pulsing, while the cathode voltage for the mosaic targets was approximately -500 V. According to fig. 7.9, at a roughly corresponding kinetic energy of 500 eV (neglecting the plasma potential [57]) the sputtering yield of aluminum is approximately 37 % higher than that of titanium; at -600 V it is even 49 % higher.

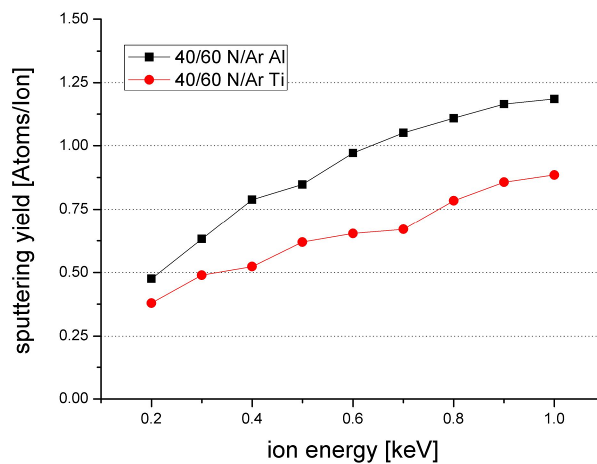

Fig. 7.9: Sputtering yield calculated by SRIM as a function of the kinetic energy of a mixture of Ar/N ions of 60:40 sputtering Al and Ti targets.

As the whole PM target consists of 60 at.% Al and 40 at.% Ti, it virtually has an aluminum matrix while the mosaic target consist of a titanium matrix with aluminum inserts (see section 6.1 and figs. 6.1a and b). Thus, the significantly higher sputtering yield of aluminum can be assumed to be responsible for the higher deposition rate obtained for the PM targets.

However, since migration and diffusion processes during film growth need energetic activation, also the energy of the film-forming neutrals sputtered from the target has an important influence on thin film growth [25, 57]. Hence, in fig. 7.10 the energy of the film-forming neutrals, again calculated by SRIM for the moment when they leave the target, is given as a function of the kinetic energy of the ions used for sputtering. Again, the data is averaged for an argon/nitrogen pressure ratio of 60:40. Obviously, the energy of the Ti neutrals is much higher than that of Al. This difference is approximately 100 % for kinetic energies of 500 eV and 600 eV. While this huge difference, at least for the moment when the species leave the target surface, might affect film growth and chemical composition (see section 7.3), it can not be used to explain the different deposition rates obtained for PM and mosaic targets.

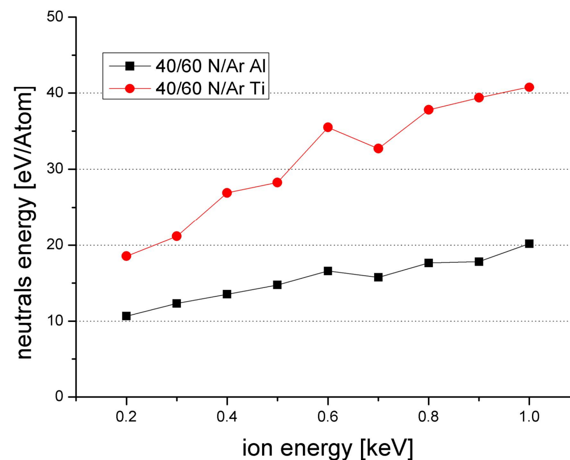

Fig. 7.10: Kinetic energy of sputtered neutrals calculated by SRIM as a function of the kinetic energy of a mixture of Ar/N ions of 60:40 sputtering Al and Ti targets.

7.3 Chemical Composition

From the series of deposition experiments done with the PM targets, those three coatings obtained at a cathode power of 7.0 kW were examined by EDX and had basically the same composition. They contained ~ 50 at.% nitrogen, ~ 31.5 at.% aluminum and ~ 18.5 at.% titanium. Consequently, the resulting Al/Ti atomic ratio was 63:37 and thus the coating composition can be written as $Ti_{0.37}Al_{0.63}N$. The Al/Ti atomic ratio is thus slightly higher than the tar-

get ratio, which is in agreement with earlier publications on sputtered coatings [72] and attributed to the higher sputtering yield of aluminum compared to titanium (see fig. 7.9).

The chemical composition of the coating grown in process R482 with the mosaic targets was ~ 51.4 at.% nitrogen, ~ 27.2 at.% aluminum and ~ 21.4 at.% titanium. Hence, the Al/Ti atomic ratio of this coating was 56:44 and the composition is $Ti_{0.44}Al_{0.56}N$. Establishing a correlation to the target composition is not possible due to the unknown effect of the arrangement of the aluminum inserts (see fig. 6.1b) on the sputtering behavior.

In summary, the investigated coatings showed compositions close to stoichiometry. The coatings deposited with the PM targets contain more aluminum than the coatings deposited with the mosaic targets which can be – according to literature [36, 72] – assumed to have a significant and positive effect on mechanical and tribological properties as well as on the oxidation behavior.

7.4 Microstructure

The grazing incidence XRD patterns of the $Ti_{1-X}Al_XN$ coatings deposited on HSS substrates using the PM targets at a cathode power of 4.5 kW and 6.0 kW are summarized in fig. 7.11. As already mentioned in subsection 6.5.3, for the given coating thicknesses in grazing incidence configuration only peaks of the coating are detected and there are no reflections of the underlying substrate material. The peak positions for cubic TiN (JCPDS 00-038-1420) and cubic AlN (JCPDS 00-025-1495) stated in the JCPDS data base are plotted as dashed lines in fig. 7.11. All coatings consist of the single-phase cubic $Ti_{1-X}Al_XN$ solid solution, as there are no peaks of the hexagonal phase recognizable. By substituting Ti atoms by smaller Al atoms in the TiN lattice, the peak is shifted to the right until it reaches the AlN peak position for 100 % AlN [45, 72]. Since the composition of the deposited coatings is approximately 60 mol% AlN and 40 mol% TiN, the detected peaks are located in between the peaks of TiN and AlN (fig. 7.11).

In fig. 7.11a, the XRD patterns for the 4.5 kW series are shown. It can be observed that the (111) peak increases with increasing total pressure. The pattern for the coating obtained in process R475 (total pressure: 550 mPa) shows a slightly higher intensity of the (200) peak at the expense of the still dominating (111) peak.

The XRD patterns for the 6.0 kW series can be seen in fig. 7.11b. The (111) peak is most pronounced for the coating grown in process R476 (total pressure: 560 mPa) and slightly less pronounced for that of process R478 (total pressure: 580 mPa). The intensity of the (111) peak of the sample synthesized by process R477 (total pressure: 540 mPa) is somewhere in

between. Additionally, it can be seen that for process R478 the (200) peak is nearly as high as the (111) oriented one.

Summarizing fig. 7.11, it can be stated that the (111) peak increases with increasing total pressure, with an only slight exception for the pattern obtained for process R478 (580 mPa, 6.0 kW).

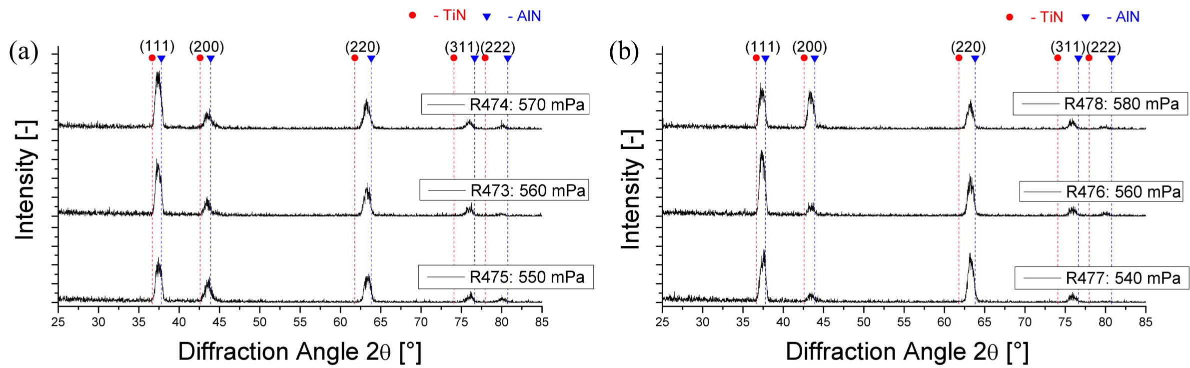

Fig. 7.11: XRD patterns obtained in grazing incidence configuration of the coatings deposited using the PM targets at (a) 4.5 kW and (b) 6.0 kW for different total pressures.

Fig. 7.12 shows the XRD patterns of the coatings deposited by the processes of the 7.0 kW series of the PM targets and by process R482 run with the mosaic targets, also at 7.0 kW. For the patterns of the 7.0 kW series, deposited from the PM targets (R479 – R481: 580 – 620 mPa), it is obvious that also here the intensity of the (111) peak increases with increasing total pressure. By comparing the pattern of the coating grown in process R482 for the mosaic targets with the patterns of the processes for the PM targets it is quite evident that the (111) peak of process R482 is less pronounced than for the other processes, while the (200) peak is predominant. Furthermore, it is apparent that the peaks of the coating grown in process R482 are slightly shifted to the left compared with the others. Such a peak shift to the left indicates compressive stress within the coating. Besides, the coating deposited in process R482 contains less aluminum (compare subsection 7.3), which also explains the peak shift towards the AlN position [45, 72].

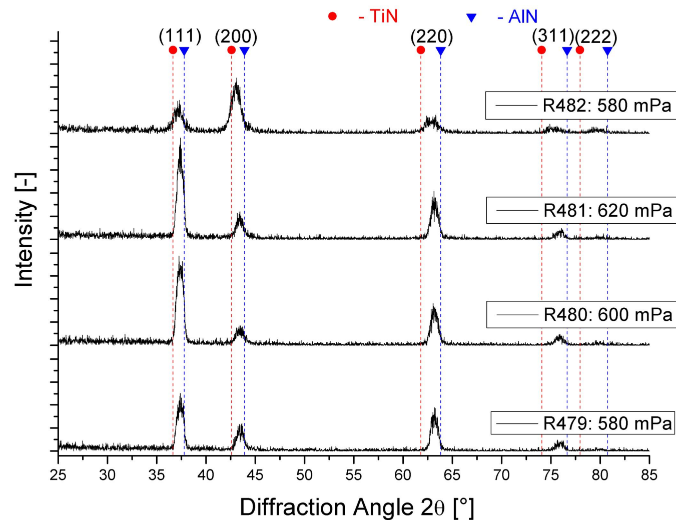

Fig. 7.12: XRD patterns obtained in grazing incidence configuration of the coatings deposited using the PM targets at different total pressures and process R482 run with mosaic targets. In all cases, the cathode power was 7.0 kW.

All observations made for the patterns derived in grazing incidence configuration are also valid for the patterns obtained in Bragg-Brentano mode.

To get more detailed information about domain size, internal strain and preferred orientation, the XRD peaks were fitted by the Pseudo-Voigt function and analyzed with the modified Harris formula (compare subsection 6.5.3).

7.4.1 Preferred Orientation

The texture coefficients of all coatings were determined by using the modified Harris formula [62, 65] with the corresponding intensities of both the AlN and the TiN reference powder samples. In fig. 7.13, the texture coefficients of the coatings of the 7.0 kW series done with the PM targets and of process R482, where the mosaic target has been used, are shown. There are no significant trends in the series of the coatings deposited with the PM targets, but there is a difference between them and the coating deposited using the mosaic targets. The outlined texture coefficients obtained for the PM targets sputtered within the 7.0 kW series are representative for the 6.0 kW and 4.5 kW series as well. The differences due to the pressure variation are very small. The preferred orientation is - as already visible in figs. 7.11 and 7.12 - the (111) orientation. The trend of vanishing (111) towards a weak (200) orientation for the mosaic targets compared to the PM targets can be seen in both plots of fig. 7.13 and is even more pronounced when using the TiN reference sample (fig. 7.13b). This difference in growth mode of the coatings deposited with PM targets and mosaic targets can be attributed to the different target materials and their different properties and, thus, to different growth conditions, which are strongly influenced by the substrate ion energy E_i and the substrate ion/atom

flux ratio J_i/J_n. Mitterer *et al.* [57] observed for TiN a phase shift from (111) to (200) orientation by increasing one or both of these variables. This trend corresponds well to the findings described above, which are related to the higher substrate current observed for the mosaic targets compared to the PM targets, as already shown in fig. 7.7, and the higher bias voltage used (see sub-sections 6.3 and 7.2.1).

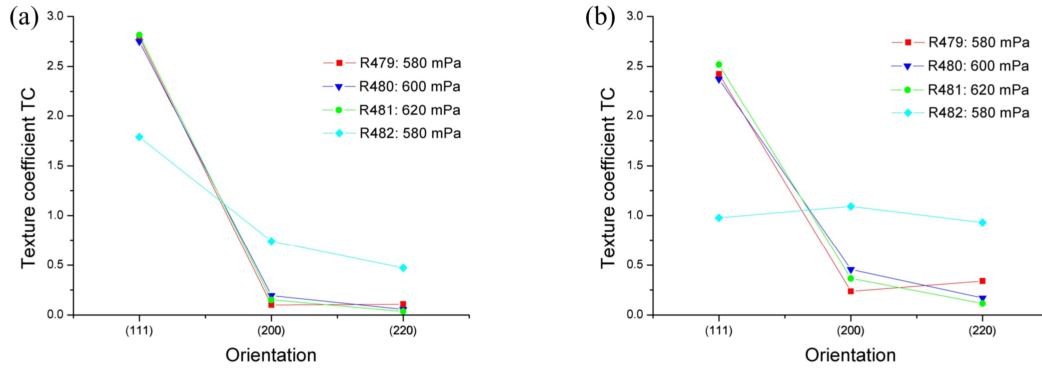

Fig. 7.13: Texture coefficients obtained for the coatings grown using the PM targets (processes R479 – 481) and the mosaic targets (process R482) with (a) AlN and (b) TiN as reference sample.

7.4.2 Domain size and Stress

To determine domain size and internal strain, the (111) peaks of the XRD patterns obtained in Bragg-Brentano mode were fitted with the Pseudo-Voigt function. Fig. 7.14 summarizes the obtained domain sizes. Basically, it can be seen that with increasing total pressure the domain size decreases. For the coating grown using the mosaic target, a by a factor of about 3 lower domain size compared to the PM targets has been found. This should again be related to the higher bias voltage and higher substrate current used for the mosaic targets, as already mentioned and discussed in sub-sections 6.3 and 7.2.1. This also corresponds well to literature [25].

The internal strain was unquantifiable small for some specimens (including R482 for the mosaic targets). For the other specimens, Hooke's law was applied.

$$\sigma = E \cdot \varepsilon \quad (7.2)$$

There, σ denotes the residual stress, E the Young's modulus and ε the internal strain. The residual stresses could be determined by using a Young's modulus of 450 GPa (see section 7.7). The resulting stresses were tensile with values between 350 -and 790 MPa. An unambiguous correlation to the varying nitrogen partial pressure or cathode power could not be found.

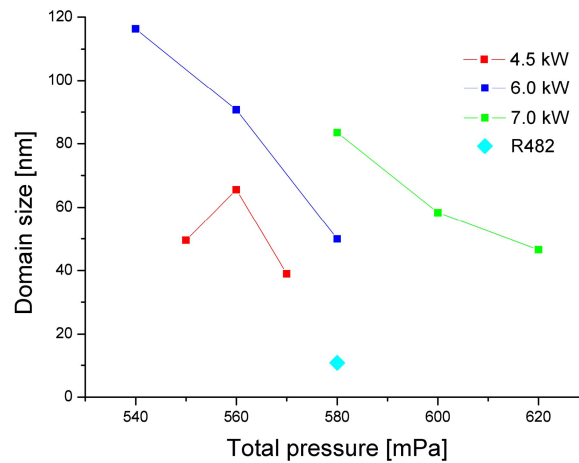

Fig. 7.14: Comparison of domain sizes obtained for the coatings grown at cathode powers of 4.5, 6.0 and 7.0 kW from the PM targets and by process R482 for the mosaic targets for different total pressures.

7.5 Coating Adhesion

The adhesion of the coating on the HSS substrates was classified according to fig. 6.5 (subsection 6.5.4). Tab. 7.2 summarizes the results of all coatings deposited from the PM targets. The coating adhesion is excellent for all coatings, as adhesion classes between HF1 and HF3 could be obtained. No significant trends could be observed. The adhesion of the coating deposited with mosaic targets on HSS was already investigated in detail by Weirather [54], where an adhesion of class HF1 was found.

Tab. 7.2: Coating adhesion classes as determined by the Rockwell C indentation test for those coatings grown using the PM targets at different cathode powers and total pressures.

Process	Cathode power [kW]	Total pressure [mPa]	Coating adhesion HF
R473	4.5	560	1
R474		570	3
R475		550	1
R476	6.0	560	2
R477		540	2
R478		580	3
R479	7.0	580	2-3
R480		600	1
R481		620	2-3

In fig. 7.15, the indents on the coatings synthesized in processes R478 and R480 representing coating adhesion classes HF3 and HF1, respectively, are shown as representative examples.

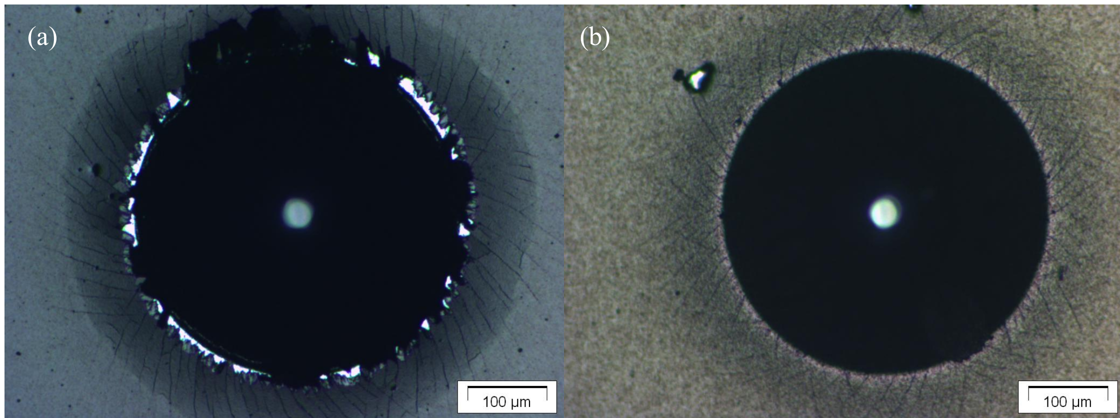

Fig. 7.15: Optical micrographs of Rockwell C indents on coatings grown in processes (a) R478 (cathode power: 6.0 kW, total pressure: 580 mPa), adhesion class HF3 and (b) R480 (cathode power: 7.0 kW, total pressure: 600 mPa), adhesion class HF1.

7.6 Residual Stress

Residual stress measurements using the wafer curvature method (see subsection 6.5.6) yielded good agreement to the results of the Pseudo-Voigt analysis. For the coatings deposited using the PM targets, tensile stresses in the range of 330 to 850 MPa were determined, which is in good agreement with the values found by fitting the XRD patterns with the Pseudo-Voigt function.

For the coating deposited using the mosaic targets (R482), compressive stresses of -975 MPa were measured, confirming the peak shift in the XRD pattern of the respective coating observed in section 7.4 (fig. 7.12). The formation of these compressive stresses is caused by the higher bias voltage used for the mosaic targets, which results in a densification of the coating microstructure [25].

7.7 Hardness and Young's Modulus

The values for the hardness and the Young's modulus, including the standard deviations, were determined for the coatings from the 7.0 kW series deposited with the PM targets and for process R482, where the mosaic targets have been used. The results are summarized in tab. 7.3. For the coatings deposited with the PM targets, there is no significant relation between the total pressure and the hardness or the Young's modulus; the values range between ~ 29 and 32 GPa for hardness and ~ 408 – 456 GPa for the Young's modulus. The highest hardness

of 35.3 ± 1.5 GPa was measured for the coating deposited in process R482 using the mosaic targets. According to fig. 7.14 (subsection 7.4.2), the domain size of this coating is significantly smaller than for the others. This indicates that the Hall-Petch effect [1, 73] plays a role. Furthermore, according to sections 7.4 and 7.6, for the coating from process R482 compressive residual stresses were determined, while for the PM coatings tensile stresses were detected. Compressive coating stresses make it more difficult for an intender to penetrate into the surface, while tensile stresses support it [74]. Therefore, apparently higher hardness values are measured for coatings with compressive stresses compared to coatings with tensile stresses [1, 73].

Tab. 7.3: Hardness and Young's modulus of those coatings synthesized at a cathode power of 7.0 kW using PM targets (processes R479 – 481) and mosaic targets (process R482).

Process	**Total pressure [mPa]**	**Hardness [GPa]**	**Young's modulus [GPa]**
R479	580	32.4 ± 2.0	455.7 ± 24.7
R480	600	29.2 ± 0.9	422.9 ± 9.0
R481	620	28.9 ± 1.5	407.9 ± 7.7
R482	580	35.3 ± 1.5	455.8 ± 23.2

7.8 Tribological Properties

Tribological investigations using a ball-on-disc test against Al_2O_3 balls were done for the 7.0 kW series using the PM targets and for process R482, where the mosaic targets have been used. The measurements were carried out at room temperature. In fig. 7.16, the development of the friction coefficient as a function of the sliding distance is shown. A running-in period of 20 to 30 m can be observed; then the friction coefficient remains more or less constant in a steady-state regime.

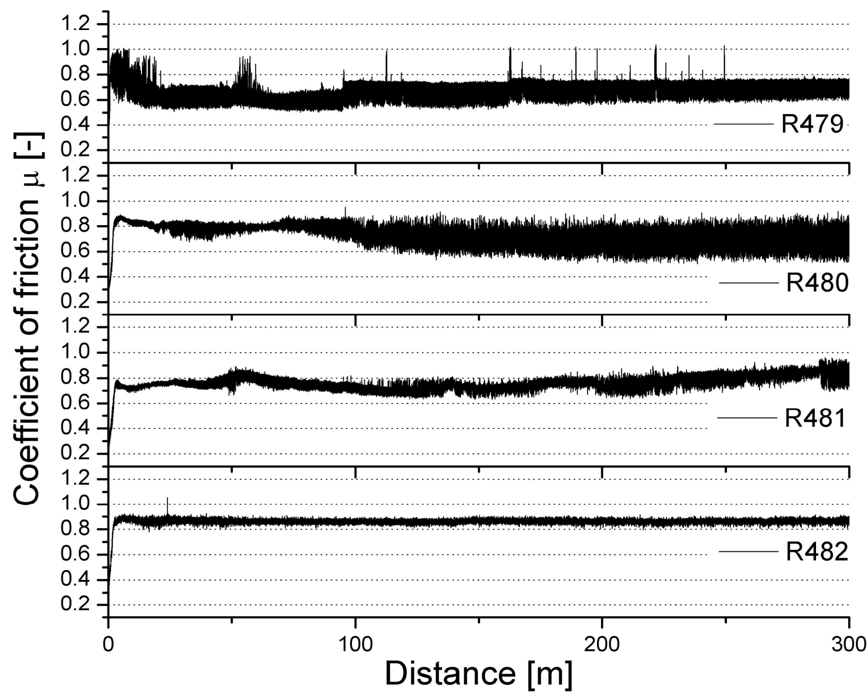

Fig. 7.16: Friction coefficient as a function of the sliding distance for the coatings obtained by processes R479 (total pressure: 580 mPa), R480 (total pressure: 600 mPa) and R481 (total pressure: 620 mPa) done using the PM targets as well as by process R482 using mosaic targets. In all cases, the cathode power was 7.0 kW.

The friction coefficients summarized in tab. 7.4 are the mean values and standard deviations determined by the InstrumX software of the tribometer, omitting the data from the running-in period. In tab. 7.4 it can be seen that the friction coefficient shows a slight increase with the total pressure for those coatings deposited from the PM targets. However, it should be mentioned that this increase is in the same range as its standard deviation and, thus, probably not very significant. The friction coefficient obtained for the coating deposited from the mosaic targets is slightly higher than those values obtained for the PM targets and in good agreement with the values of Weirather [54].

Tab. 7.4: Friction coefficients of those coatings synthesized at a cathode power of 7.0 kW using PM targets (processes R479 – 481) and mosaic targets (process R482).

Process	**Total pressure [mPa]**	**Friction coefficient μ [-]**
R479	580	0.68 ± 0.06
R480	600	0.73 ± 0.08
R481	620	0.76 ± 0.06
R482	580	0.86 ± 0.03

In fig. 7.17, 3D views of the wear tracks are shown. At room temperature, the dominating wear mechanism is abrasive wear caused by micro-plowing and micro-cutting [28, 32]. Especially in fig. 7.17b and c the thereby arisen grooves can be identified. The wear coefficient was calculated for all four specimens (compare subsection 6.5.7). The results are shown in tab. 7.5. The wear track of the coating grown by process R479 (fig. 7.17a) appears very smooth, which corresponds to the obtained friction (tab. 7.4) and wear coefficient (tab. 7.5) which are both the lowest ones obtained. The wear track of the coating from process R482 deposited from the mosaic targets does also not show very pronounced abrasion grooves, although it exhibits the highest friction coefficient as well as the highest wear coefficient. The obtained wear coefficients confirm what already could be concluded from the 3D views of the wear tracks. The wear coefficient increases with increasing total pressure for those coatings deposited using the PM targets. The wear coefficient obtained for the coating deposited from the mosaic targets is slightly higher than those obtained for the coatings deposited from the PM targets, but it corresponds – as also the friction coefficient – well to the results of Weirather [54]. Kutschej *et al*. [72] obtained slightly higher values for the friction as well as the wear coefficient. This can be attributed to the low normal load (1 N) used there, which has been reported to result in significantly higher friction coefficients [75]. Furthermore, also the humidity during the test can be assumed to influence the friction coefficient. The tribological investigations of Kutschej *et al*. were done at a relative humidity of 40 – 50 %, while the investigations within this thesis were done at 27 ± 1 % (compare subsection 6.5.7).

Tab. 7.5: Wear coefficients of those coatings synthesized at a cathode power of 7.0 kW using PM targets (processes R479 – 481) and mosaic targets (process R482).

Process	**Total pressure [mPa]**	**Wear coefficients [m³/Nm]**
R479	580	$7.69 \cdot 10^{-15}$
R480	600	$9.84 \cdot 10^{-15}$
R481	620	$1.03 \cdot 10^{-14}$
R482	580	$1.04 \cdot 10^{-14}$

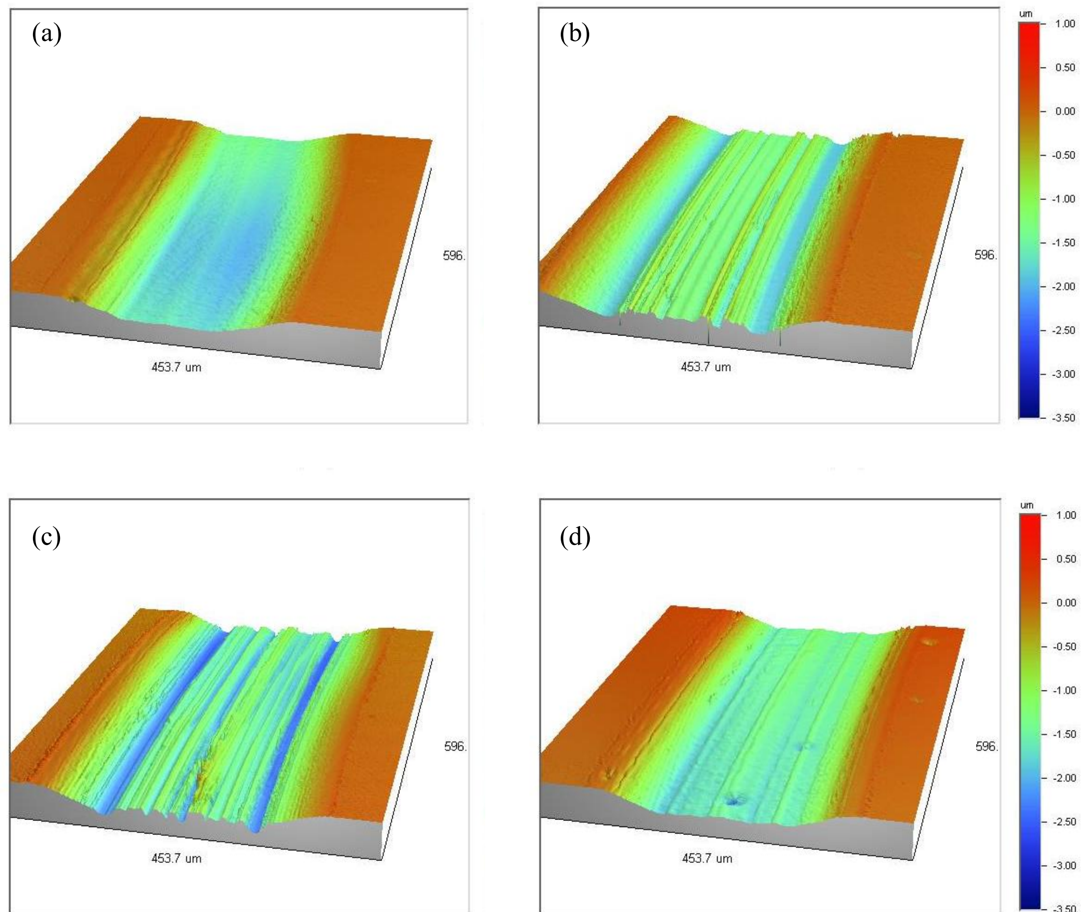

Fig. 7.17: 3D view of the wear tracks of the coatings synthesized in processes (a) R479 (total pressure: 580 mPa), (b) R480 (total pressure: 600 mPa), (c) R481 (total pressure: 620 mPa) done using the PM targets as well as process (d) R482 using the mosaic targets. In all cases, the cathode power was 7.0 kW.

8 Summary and Conclusions

Within this thesis, powder metallurgical and mosaic TiAl targets for sputter deposition of $Ti_{1-X}Al_XN$ hard coatings were compared with respect to the coating process and some characteristics of the obtained coatings. In pursuit of this goal, $Ti_{1-X}Al_XN$ coatings were deposited on high speed steel substrates by reactive unbalanced magnetron sputtering. As with the utilized industrial-size sputter device mosaic targets with aluminum inserts arranged in a titanium target have been used, a well established standard deposition process was available, while for the powder metallurgical targets with an Al/Ti atomic ratio of 60:40 first of all the deposition process had to be optimized. For that reason, variations of the target sputter power and the nitrogen partial pressure have been done. It became apparent that in order to run a stable process with the same cathode power as with the mosaic targets, a 7 % higher nitrogen partial pressure was required than for the mosaic targets.

The implemented sputter process for the powder metallurgical targets was compared to the commercially applied mosaic target process by taking into account the sputtering yields of titanium and aluminum and the respective deposition rates. The deposition rate obtained with the mosaic targets was approximately 44 % lower than that of the powder metallurgical targets. This is mainly due to the different target materials and therefore different sputtering yields. The powder metallurgical targets consist of an aluminum matrix with titanium grains embedded, while the mosaic targets consist of a titanium matrix with aluminum filled holes. The Monte Carlo based SRIM software was used to simulate the sputter process and to clarify the differences in sputtering yield. The calculations indicated that the sputtering yield of aluminum in an argon/nitrogen mixture of 60/40 is, depending on the ion energy, approximately 37 - 49 % higher than that of titanium.

At constant total process pressure, the mosaic targets showed a slightly higher target current which indicates a higher sputter erosion rate. On the other hand, in the given commercial process with the mosaic targets the bias voltage was slightly higher than that used for the powder metallurgical targets, indicating that re-sputtering might play a role which reduces the deposition rate. A further reduction of the deposition rate might result from the higher substrate current occurring in the mosaic target process, which originates from the higher bias voltage and also from the higher cathode currents. Therefore, the advantage of the higher target current and the disadvantage of the higher bias voltage and substrate current seem to compensate each other.

The usable thickness of the powder metallurgical targets is 66 % higher than that of the mosaic targets. Therefore, the acceptable erosion track of the powder metallurgical targets can be deeper and consequently the target lifetime is longer.

The coatings deposited from the mosaic targets contained less aluminum than the coatings deposited from the powder metallurgical targets. The actual aluminum to titanium atomic ratio of the coatings deposited with the powder metallurgical targets was 63/37 and lies slightly above the target composition, while for the coatings deposited with the mosaic targets it was 56/44.

All coatings consisted of single phase cubic $Ti_{1-X}Al_XN$ solid solution. The coatings deposited from the powder metallurgical targets exhibit a (111) preferred orientation, while the coating from the mosaic targets showed a trend towards a (200) orientation. With increasing nitrogen partial pressure for the coatings deposited with the powder metallurgical targets, the domain size of the $Ti_{1-X}Al_XN$ phase decreased. The domain size of the coating deposited with the mosaic targets was significantly smaller than for the coatings synthesized using the powder metallurgical targets. While for the coating deposited with the mosaic targets compressive stresses were determined, tensile stresses were obtained for the coatings grown from the powder metallurgical targets. The differences in domain size, preferred orientation and stress could be related to the slightly more intense and energetic ion bombardment conditions used in the mosaic target process.

The hardness of the coating deposited with the mosaic targets was slightly higher than that of the coatings synthesized with the powder metallurgical targets. This can be attributed to the smaller domain size and, therefore, to the Hall-Petch hardening effect as well as to the compressive residual stresses. Coating adhesion was excellent in all cases.

Tribological investigations revealed that both the friction coefficients and the wear coefficients were slightly lower for the coatings deposited with the powder metallurgical targets.

In conclusion, the investigations showed that by sputtering from powder metallurgical targets coatings with comparable properties to those deposited with mosaic targets could be grown in less deposition time and with longer target lifetime. Already after obtaining this relatively early stage of knowledge, the coatings grown from the powder metallurgical targets show lower friction coefficients and higher wear resistance, where the latter might be related to their higher aluminum contents. Nevertheless, there seems to be further potential for improving these coatings, most promising by turning their stress state from tensile to compressive by optimizing the substrate ion bombardment conditions.

Bibliography

[1] P.H. Mayrhofer, C. Mitterer, L. Hultman, H. Clemens, Microstructural design of hard coatings, Progr. Mater. Sci. 51, 1032-1114, 2006.

[2] K. Bobzin, N. Bagcivan, P. Immich, S. Bolz, R. Cremer, T. Leyendecker, Mechanical properties and oxidation behaviour of (Al,Cr)N and (Al,Cr,Si)N coatings for cutting tools deposited by HPPMS, Thin Solid Films 517, 1251-1256, 2008.

[3] Fr.-W. Bach, T. Duda, Moderne Beschichtungsverfahren, Wiley-VCH, Weinheim, 2000.

[4] R. F. Bunshah, Deposition technologies for films and coatings, Noyes Publications, New Jersey, 1982.

[5] R. A. Haefer, Oberflächen- und Dünnschicht-Technologie, Teil I, Beschichtungen von Oberflächen, Springer Verlag, Berlin, Heidelberg, 1987.

[6] B. Rother, J. Vetter, Plasmabeschichtungsverfahren und Hartstoffschichten, Deutscher Verlag für Grundstoffindustrie, Leipzig, 1992.

[7] H. Frey, Vakuumbeschichtung 1, Plasmaphysik – Plasmadiagnostik – Analytik, VDI Verlag, Düsseldorf, 1995.

[8] G. Kienel, Vakuumbeschichtung 4, Anwendungen Teil I, VDI Verlag, Düsseldorf, 1993.

[9] M. Griepentrog, B. Machrodt, G. Mark, T. Linz, Properties of TiN hard coatings prepared by unbalanced magnetron sputtering and cathodic arc deposition using a uni- and bipolar pulsed bias voltage, Surf. Coat. Technol. 74-75, 326-332, 1995.

[10] E. Lugscheider, O. Knotek, F. Löffler, C. Barimani, S. Guerreiro, H. Zimmermann, Deposition of arc TiAlN coatings with pulsed bias, Surf. Coat. Technol. 76-77, 700-705, 1995.

[11] G. Reiners, M. Griepentrog, Hard coatings on magnesium alloys by sputter deposition using a pulsed d.c. bias voltage, Surf. Coat. Technol. 76-77, 809-814, 1995.

[12] J.N. Matossian, R. Wei, J.D. Williams, Plasma-based ion implantation and electron-bombardment for large-scale surface modification of materials, Surf. Coat. Technol. 96, 58-67, 1997.

[13] H.C. Barshilia, K.S. Rajam, Reactive sputtering of hard nitride coatings using asymmetric-bipolar pulsed DC generator, Surf. Coat. Technol. 201, 1827-1835, 2006.

[14] D. Carter, H. Walde, G. McDonough, G. Roche, Parameter optimization in pulsed DC reactive sputter deposition of aluminum oxide, Proc. Conf. Society of Vacuum Coaters 505/856-7188, 2002.

[15] M. Ohring, The materials science of thin films – deposition and structure, Academic Press, San Diego, Second edition, 2002.

[16] R.D. Arnell, P.J. Kelly, Recent advances in magnetron sputtering, Surf. Coat. Technol. 112, 170-176, 1999.

[17] P.H. Mayrhofer, Materials science aspects of nanocrystalline PVD hard coatings, PhD Thesis, Montanuniversität Leoben, 2001.

[18] J. L. Vossen, W. Kern, Thin film processes II, Academic Press, San Diego, 1991.

[19] D. Depla, R. De Gryse, Target poisoning during reactive magnetron sputtering: Part I: The influence of ion implantation, Surf. Coat. Technol., 184-189, 2003.

[20] M. Moser, Structural evolution of protective coatings for gamma-TiAl based alloys, PhD Thesis, Montanuniversität Leoben, 2008.

[21] R. Messier, A.P. Giri, R.A. Roy, Revised structure zone model for thin film physical structure, J. Vac. Sci. Technol. A, 2(2), 500-503, 1984.

[22] B.A. Movchan, A.V. Demchishin, Study of the structure and properties of thick vacuum condensates of nickel, titanium, tungsten, aluminum oxide and zirconium dioxide, Phys. Met. Metallogr. 28, 653-660, 1969.

[23] J.A. Thornton, Influence of apparatus geometry and deposition conditions on the structure and topography of thick sputtered coatings, J. Vac. Sci. Technol. 11(4), 666 – 670, 1974.

[24] P.B. Barna, M. Adamik, Fundamental structure forming phenomena of polycrystalline films and the structure zone models, Thin Solid Films 317, 27 – 33, 1998.

[25] I. Petrov, P.B. Barna, L. Hultman, J.E. Greene, Microstructural evolution during film growth, J. Vac. Sci. Technol. 21(5), 117 – 128, 2003.

[26] P.B. Barna, M. Adamik, Formation and characterization of the structure of surface coatings, in Y. Pauleau and P.B. Barna, editors, Protective Coatings and Thin Films, 279-297, Kluwer Academic Publishers, Dordrecht, 1997.

[27] G.W. Stachowiak, A.W. Batchelor, Engineering tribology, Butterworth-Heinemann, Woburn, 2001.

[28] K. Holmberg, A. Matthews, Coatings tribology, properties, techniques and applications in surface engineering, Elsevier Science, Amsterdam, 1994.

[29] P.J. Blau, Friction and wear transitions of materials, Noyes Publications, New Jersey, 1989.

[30] I.M. Hutchings, Tribology: Friction and wear of engineering materials, Edward Arnold, London, 1992.

[31] N.P. Suh, H.-C. Sin, The genesis of friction, Wear 69, 91-114, 1981.

[32] E. Rabinowicz, Friction and wear of materials, 2nd edition, John Wiley & Sons, New York, 1995.

[33] V. Valvoda, Structure of thin films of titanium nitride, J. Alloys Compd. 219, 83-87, 1995.

[34] G. Zhang, B. Li, B. Jiang, F. Yan, D. Chen, Microstructure and tribological properties of TiN, TiC, Ti(C, N) thin films prepared by closed-field unbalanced magnetron sputtering ion plating, Appl. Surf. Sci. 255, 8788-8793, 2009.

[35] W.D. Münz, Titanium aluminium nitride films: A new alternative to TiN coatings, J. Vac. Sci. Technol. 4(6), 2717-2725, 1986.

[36] S. PalDey, S.C. Deevi, Single layer and multilayer wear resistant coatings of (Ti, Al)N: A review, Mat. Sci. Eng. 342, 58-79, 2003.

[37] I.-W. Park, D.S. Kang, J.J. Moore, S.C. Kwon, J.J. Rha, K.H. Kim, Microstructures, mechanical properties, and tribological behaviors of Cr-Al-N, Cr-Si-N, and Cr-Al-N coatings by a hybrid coating system, Surf. Coat. Technol. 201, 5223-5227, 2007.

[38] E. Spain, J.C. Avelar-Batista, M. Letch, J. Housden, B. Lerga, Characterization and applications of Cr-Al-N coatings, Surf. Coat. Technol. 200, 1507-1513, 2005.

[39] M. Zhou, Y. Makino, M. Nose, K. Nogi, Phase transition and properties of Ti-Al-N thin films prepared by r.f.-plasma assisted magnetron sputtering, Thin Solid Films 339, 203-208, 1999.

[40] H.A. Jehn, B. Rother, Preparation and concentration distribution of multicomponent hard coatings, Int. J. Refract. Metals Hard Mater. 14, 87-95, 1996.

[41] J. Kohlscheen, H.-R. Stock, P. Mayr, Substoichiometric titanium nitride coatings as machinable surfaces in ultraprecision cutting, Surf. Coat. Technol. 120-121, 740-745, 1999.

[42] M. Durandurdu, Pressure-induced phase transition of zinc-blende AlN: An ab initio molecular dynamic study, J. Phys. Chem. Solids, 69, 11, 2894-2897, 2008.

[43] R. Cremer, M. Witthaut, D. Neuschütz, Experimental determination of the metastable (Ti,Al)N phase diagram up to 700 °C, in W.D. Cho, H.Y. Sohn, editors, Value-Addition Metallurgy, The Minerals, Metals & Materials Society, Warrendale, 1998.

[44] H. Holleck, Metastable coatings – prediction of composition and structure, Surf. Coat. Technol. 36, 151-159, 1988.

[45] A. Kimura, H. Hasegawa, K. Yamada, T. Suzuki, Effects of Al content on hardness, lattice parameter and microstructure of $Ti_{1-x}Al_xN$ films, Surf. Coat. Technol. 120-121, 438-441, 1999.

[46] P.H. Mayrhofer, F.D. Fischer, H.J. Böhm, C. Mitterer, J.M. Schneider, Energetic balance and kinetics for the decomposition of supersaturated $Ti_{1-x}Al_xN$, Acta Materialia 55, 1441-1446, 2007.

[47] A. Hörling, L. Hultman, M. Odén, J. Sjölén, L. Karlsson, Thermal stability of arc evaporated high aluminum content $Ti_{1-x}Al_xN$ thin films, J. Vac. Technol. 20(5), 1815-1823, 2002.

[48] P.H. Mayrhofer, A. Hörling, L. Karlsson, J. Sjölén, T. Larsson, C. Mitterer, L. Hultman, Self-organized nanostructures in the Ti-Al-N system, Appl. Phys. Lett. 83(10), 2049-2051, 2003.

[49] K.-L. Lin, M.-Y. Hwang, C.-D. Wu, The deposition and wear properties of cathodic arc plasma deposition TiAlN deposits, Mater. Chem. Phys. 46, 77-83, 1996.

[50] R. Wuhrer, W.Y. Yeung, A comparative study of magnetron co-sputtered nanocrystalline titanium aluminium and chromium aluminium nitride coatings, Scripta Mater. 50, 1461-1466, 2004.

[51] L. Chen, M. Moser, P.H. Mayrhofer, Compositional and structural evolution of sputtered Ti-Al-N, Thin Solid Films 517, 6635-6641, 2009.

[52] H. Ohnuma, N. Nihira, A. Mitsuo, K. Toyoda, K. Kubota, T. Aizawa, Effect of aluminium concentration on friction and wear properties of titanium aluminium nitride films, Surf. Coat. Technol. 177-178, 623-626, 2004.

[53] P.C. Jindal, A.T. Santhanam, U. Schleinkofer, A.F. Shuster, Performance of PVD TiN, TiCN and TiAlN coated cemented carbide tools in turning, Int. J. Refract. Metals Hard Mater. 17, 163-170, 1999.

[54] T. Weirather, Hochtemperaturbeschichtung von $Ti_{1-X}Al_XN$ auf verschiedenen Schnellarbeitsstählen, Diplomarbeit, Montanuniversität Leoben, 2008.

[55] Böhler Edelstahl GmbH & Co KG, http://www.bohler-edelstahl.com/, June 2010.

[56] J.F. Ziegler, M.D. Ziegler, J.P. Biersack, SRIM – the stopping and range of ions in matter, Version SRIM-2008.04, www.SRIM.org.

[57] C. Mitterer, P.H. Mayrhofer, E. Kelesoglu, R. Wiedemann, H. Oettel, Internal growth parameters – a suitable basis for comparison of PVD coatings, Z. Metallkde. 90(8) 602-607, 1999.

[58] G. Kienel, Vakuumbeschichtung 3, Anlagenautomatisierung – Meß- und Analysentechnik, VDI Verlag, Düsseldorf, 1994.

[59] M. Birkholz, Thin film analysis by x-ray scattering, Wiley-VCH, Weinheim, 2006.

[60] Siemens D500/501, Operating Manual.

[61] Th.H. De Keijser, J.I. Langford, E.J. Mittemeijer, A.B.P. Vogels, Use of the Voigt function in a single-line method for the analysis of X-ray diffraction line broadening, J. Appl. Cryst. 15, 308-314, 1982.

[62] G.B. Harris, Quantitative measurement of preferred orientation in rolled uranium bars, Phil. Mag. 43, 113-123, 1952.

[63] I. Iordanova, P.J. Kelly, R. Mirchev, V. Antonov, Crystallography of magnetron sputtered TiN coatings on steel substrates, Vacuum 81, 830-842, 2007.

[64] M.I. Jones, I.R. McColl, D.M. Grant, Effect of substrate preparation and deposition conditions on the preferred orientation of TiN coatings deposited by RF reactive sputtering, Surf. Coat. Technol. 132, 143-151, 2000.

[65] M.H. Müller, W.P. Chernock, P.A. Beck, Comments on inverse pole figure methods, Trans. Metallurgical Society AIME 212, 39-40, 1958.

[66] H.-R. Stock, A. Schulz, DIN-Fachbericht 39: Charakterisierung dünner Schichten, 1. Auflage, in H. Jehn, G. Reiners, N. Siegel, editors, Beuth Verlag, Berlin, 1993.

[67] R. Saha, W.D. Nix, Effects of the substrate on the determination of thin film mechanical properties by nanoindentation, Acta Mater. 50, 23-38, 2002.

[68] W.C. Oliver, G.M. Pharr, An improved technique for determining hardness and elastic modulus using load displacement sensing indentation experiments, J. Mater. Res. 7(6), 1564-1583, 1992.

[69] D. Winkler, Konzeption und Realisierung eines thermisch unterstützten Meßverfahrens zur Bestimmung von Eigenspannungen in dünnen Schichten, Diplomarbeit, Montanuniversität Leoben, 1997.

[70] D. Depla, A. Colpaert, K. Eufinger, A. Segers, J. Haemers, R. De Gryse, Target voltage behaviour during DC sputtering of silicon in an argon/nitrogen mixture, Vacuum 66, 9-17, 2002.

[71] P. Losbichler, C. Mitterer, Non-reactively sputtered TiN and TiB_2 films: Influence of activation energy on film growth, Surf. Coat. Technol. 97, 567-573, 1997.

[72] K. Kutschej, P.H. Mayrhofer, M. Kathrein, P. Polcik, R. Tessadri, C. Mitterer, Structure, mechanical and tribological properties for sputtered $Ti_{1-X}Al_xN$ coatings with $0.5 \leq x \leq 0.75$, Surf. Coat. Technol. 200, 2358-2365, 2005.

[73] P.H. Mayrhofer, C. Mitterer, J. Musil, Structure-property relationships in single- and dual-phase nanocrystalline hard coatings, Surf. Coat. Technol. 174-175, 725-731, 2003.

[74] P.H. Mayrhofer, Übungen zu Werkstoffprüfung, in M. Panzenböck, editor, Lecture Script, 4. Auflage, Montanuniversität Leoben, 2003.

[75] S.-Y. Yoon, J.-K. Kim, K.H. Kim, A comparative study on tribological behavior of TiN and TiAlN coatings prepared by arc ion plating technique, Surf. Coat. Technol. 161, 237-242, 2002.